Meteorologische Zeitschrift, Vol. **24**, No. 3, 269–292 (published online April 4, 2015)
© 2015 The authors

Article

Goal-oriented adaptivity for idealised tropical cyclones: A binary interaction scenario

Martin Baumann[1*], Vincent Heuveline[1], Leonhard Scheck[2] and Sarah C. Jones[3]

[1]Engineering Mathematics and Computing Lab, Interdisciplinary Center for Scientific Computing, Heidelberg University, Heidelberg, Germany
[2]Institute for Meteorology and Climate Research, Karlsruhe Institute of Technology, Karlsruhe, Germany. Current affiliation: Hans-Ertel-Centre for Weather Research, Ludwig-Maximilians-Universität München, Germany
[3]Deutscher Wetterdienst, Offenbach, Germany

(Manuscript received February 18, 2014; in revised form December 2, 2014; accepted December 3, 2014)

Abstract

Forecasting the motion and evolution of tropical cyclones is a challenging, computationally expensive task. Complex, interacting physical processes on a wide range of scales need to be considered. Adaptive techniques, such as local mesh refinement, are a promising way to improve the efficiency of numerical models for such multi-scale problems. We investigate the interaction of two tropical cyclones in a barotropic model assuming exact initial conditions and discuss how the impact of discretization errors on the prediction of storm tracks can be minimized using adjoint-based goal-oriented adaptivity. We propose suitable functionals for the prediction of storm tracks, interpret the associated sensitivity from a meteorological point of view and discuss its relation to sensitivity measures commonly used in meteorological applications. We present numerical results of adaptive simulations on optimized meshes and adaptive time stepping controlled by a posteriori error estimators that exploit the sensitivity information. Using goal-oriented adaptivity, the storm tracks can be determined about one order of magnitude more precisely, compared to uniform discretizations with the same number of unknowns. The highest improvement in accuracy (up to two orders of magnitude) can be observed for meshes with comparatively low number of cells.

Keywords: goal-oriented space-time finite element method, a posteriori error estimation, automatic grid refinement, adjoint sensitivity, sensitivity analysis, tropical cyclone dynamics

1 Introduction

The accurate prediction of the motion and evolution of tropical cyclones (TCs) is a challenging problem for numerical weather prediction, because interacting physical processes on a wide range of scales have to be considered. Processes on convective scales in the inner core of the cyclone determine the intensity evolution and thus the storm's influence on larger scales. The motion of a TC is mainly determined by the large scale flow and influences its environment, which in turn has a strong impact on the convective processes in the core. Forecasting the development of TCs is thus a multiscale problem.

Performing TC forecast model runs on uniform grids with a sufficiently high resolution to resolve the inner core dynamics and on a domain sufficiently large to contain the relevant scale flow features leads to high computational costs. Adaptive mesh refinement techniques have been used in previous work to reduce the computational effort. The most common approach is to embed a high-resolution grid nest containing the core of the storm in a coarser grid (see e.g. Birchfield 1960 and Harrison and Elsberry 1972). Current models often use multiple nests around the storm center. For instance, in the Advanced Hurricane WRF model nested grids with resolutions of 12 km, 4 km and 1.33 km are centered on the storm and follow its motion (Cavallo et al., 2013; Davis and Holland, 2007).

While these nesting approaches certainly present a huge improvement over uniform grids, they are unlikely to result in optimal efficiency. Usually the number, size and resolution of the grid nests is not changed during a model run. In general, they will include regions that are not important for the outcome of the forecast. On the other hand, there may be remote features on the coarse grid outside of the high-resolution nests that have a strong impact on the motion and evolution of the storm. For instance, by means of a linear sensitivity analysis it has been shown that for TCs interacting with the mid-latitude flow perturbations several 1000 km upstream can have a large impact on the storm within 48 hours (Reynolds et al., 2009; Peng and Reynolds, 2006; Scheck et al., 2013). A higher grid resolution in such remote sensitive regions could improve the accuracy of the forecast.

Ideally, grid refinement methods should automatically determine where and how strongly the grid should

*Corresponding author: Martin Baumann, Engineering Mathematics and Computing Lab, Interdisciplinary Center for Scientific Computing, Heidelberg University, Speyerer Str. 6, 69115 Heidelberg, Germany, e-mail: martin.baumann@uni-heidelberg.de

© 2015 The authors

be refined or coarsened to achieve optimal efficiency. For a barotropic TC forecast model, Fulton (2001) used truncation error estimates obtained with a multigrid approach to control the grid refinement automatically. Similarly, a posteriori error estimation based on global norms can be used to control grid adaptation, for an overview see e.g. Ainsworth and Oden (2000). These methods aim at reducing the instantaneous, global discretization error. However, the goal of a TC forecast is primarily to predict the position, structure and intensity of the storm at the forecast time, which is typically several days in the future. It would be advantageous if the automatic grid optimization process would take these specific goals into account. This implies that not only the instantaneous discretization error, but also its time evolution and its impact on the specific goals should be considered in the adaptation process.

The Dual Weighted Residual (DWR) method represents a generic framework for goal-oriented error control. It goes back to Eriksson et al. (1995) and has been used successfully in many fields of application, for instance for fluid flow with chemical reactions, cf. Braack and Rannacher (1999), or for investigations of hydrodynamic stability, cf. Heuveline and Rannacher (2006). The main idea of the DWR method is to adapt a discretization in a way that minimizes the error in a *goal functional*, denoted by J, which is assumed to describe the most important aspect of the investigated problem. In this case, $J(u)$ should be determined with high precision, where u denotes the solution of the original problem denoted the *primal problem* in this context. The corresponding *dual problem* can be derived introducing a Lagrange functional (similar as for problems of constraint optimization). It is defined by means of the adjoint of the primal problem's linearised operator and is posed backward in time (see Bangerth and Rannacher (2003) for details). The solution of the dual problem represents the sensitivity of the functional J with respect to perturbations of the primal problem's solution u. Based on this linear sensitivity analysis, the DWR method provides an estimator for the quantification of the error $J(u) - J(u_h)$, where u_h is a Galerkin approximation of the continuous solution u (which is a usual situation in the context of finite element methods, for example). From this estimation, the distribution of local error contributions can be determined and results in cell-wise *error indicators*, based on which cells can be marked that should be refined or coarsened to balance the error contributions over all cells.The overall procedure of the DWR method, which is an iterative process, is illustrated in Fig. 1. In each adaptation cycle, the primal problem is solved on the current mesh for the complete time interval $[0, T]$, followed by the solution of the dual problem, which is posed backward in time. Subsequently, the error in J is estimated, corresponding error indicators are derived, and finally the mesh is adapted. This cycle is repeated until the desired accuracy is achieved. For many applications, highly efficient meshes have been constructed using the DWR method

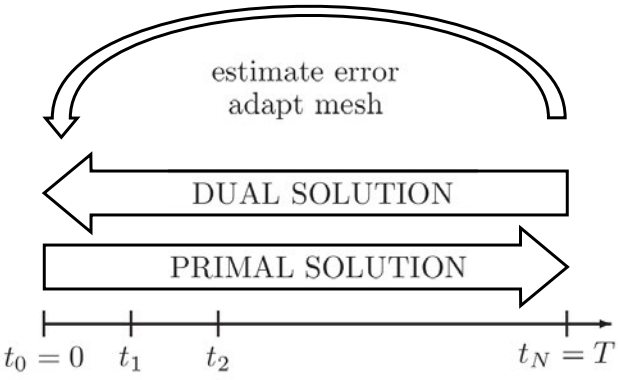

Figure 1: Calculations done in each iteration loop of the Dual Weighted Residual method: Solution of primal and dual problem, evaluation of error estimator, and mesh adaptation.

(as described e.g. in the aforementioned references) in the sense that the error of a corresponding numerical solution, measured in the functional J, is significantly smaller compared to the error of a numerical solution on a uniform meshes with the same number of unknowns.

Since the DWR method allows to optimize the discretization with respect to user-defined, specific features of a problem, it represents a promising approach for the multi-scale problem of forecasting the development of TCs. As a first step towards the operational application of this method, we apply the DWR method to an idealized TC scenario in this study. As a test case, we model the interaction of two TCs in a non-divergent barotropic framework and investigate how the efficiency in the storm track prediction can be improved. The binary TC interaction is a challenging test problem for grid adaptation, as the solution is very sensitive not only to changes in the initial conditions, but also to numerical errors. A shallow-water version of this problem has already been used by Bauer et al. (2014) as a test case for r-adaptive methods, in which the mesh is adapted by moving grid points. They investigated how error indicators can be applied to control r-adaptation and demonstrated that error estimations can successfully be used to control the grid refinement in a model that makes use of differing but related model equations. Bauer et al. (2014) computed the error estimators on a uniform grid and performed only one DWR step to adapt the grid.

For this study we apply the full iterative DWR method and focus on the more flexible h-adaptivity approach. We use a space-time finite element method as discretization which guarantees that resulting solutions have a Galerkin property with respect to the time and the space dimension. We apply a specialized version of the goal-oriented error estimator that allows for the estimation of the temporal and the spatial discretization error. To the knowledge of the authors, the investigated discretization scheme applied to the primal and dual problem and the corresponding goal-oriented error estimator have not been discussed in the literature. Therefore, we provide a very detailed description of the steps of dis-

cretization and the evaluation of the error estimator. We propose several meteorologically motivated goal functionals that aim at minimizing the error in the storm position and calculate the corresponding sensitivity information in form of the dual solution. It is a unique advantage of the DWR approach that this sensitivity information is generated as a free by-product of the error estimation process. We provide a general physical interpretation of the dual solution and discuss its connection to sensitivity measures commonly used for meteorological applications, like singular vectors and adjoint based sensitivity. The structure of the dual solution for the binary TC interaction problem is interpreted using results of a recent study on the growth of optimal perturbations for vortices in shear flows. We present results of adaptive numerical model runs for which the spatial mesh and also the time partitioning is optimized according to goal-oriented error indicators for the proposed functionals. The mesh structure and the accuracy of the solution for the different goal functionals are discussed. Finally, we evaluate the efficiency of the adaptive approach, compared to model runs on uniform grids.

This article is organized as follows: In Section 2, we define the idealized binary cyclone interaction test problem and several physically motivated goal functionals. The primal and dual problems and a corresponding space-time finite element discretizations are introduced in Section 3. Details on error estimation and adaptation strategies are specified in Section 4. In Section 5, we give a physical interpretation of the dual solution and discuss its structure for the binary cyclone scenario. In Section 6, adaptive numerical runs are presented and compared to simulations on uniform discretizations. Finally, we summarize our results and discuss open questions in Section 7.

2 Scenario and goal functionals

2.1 A binary cyclone interaction scenario

The interaction of tropical cyclones takes place on average about two times per year (Dong and Neumann, 1983), often leads to complex cyclone tracks (Lander and Holland, 1993) and can increase the forecast error significantly (Brand, 1970; Jarrell et al., 1978). The cyclones advect each other mutually and the shear of their circulations induces changes in the vortex structure and can lead to the formation of filaments. First investigations on this process were carried out by Fujiwhara (1921); Fujiwhara (1923); Fujiwhara (1931), who showed in laboratory experiments that two vortices approached each other in a spiral orbit and merged, when their initial separation was sufficiently small.

Several studies using idealized, in most cases barotropic, models were carried out to investigate these processes further. This vortex interaction problem is relevant not only for tropical cyclones, but also for two-dimensional turbulence. Melander et al. (1988) carried out model runs for the symmetric case (i.e. two identical vortices) and explained the merging of the vortices as the result of an inviscid axi-symmetrization process similar to the one occurring for a single elliptically deformed vortex (Melander et al., 1987). Dritschel and Waugh (1992) considered the interaction of unequal vortices and showed that in addition to mergers and elastic interactions other outcomes are possible. These include partial mergers and cases in which one of the vortices is partially or completely converted into filaments. Prieto et al. (2003) performed a similar study but considered also spherical geometry and thus β effects. Ritchie and Holland (1993) and Holland and Dietachmayer (1993) consider, in contrast to the studies mentioned so far, vortices including fluid with negative vorticity at larger radii. The negative vorticity leads to a faster decay of the tangential velocity with radius, in better agreement with real TC wind fields. Ritchie and Holland (1993) derive an expression for the approximate maximum distance required for a rapid merger, which lies in the range of 150–300 km. Shin et al. (2006) discuss the relation between the critical distance and the vorticity structure between the vortices.

Here we restrict ourselves to the symmetric case and investigate the interaction of two identical vortices in a non-divergent barotropic model[1]. We consider a case similar to the ones explored in Richter (2012). For the vortices we assume a tangential velocity profile introduced by Smith et al. (1990), which is given as

$$v_T(s) = v_0 \frac{s(1 + (6b/2a)s^4)}{(1 + as^2 + bs^6)^2}, \tag{2.1}$$

where $s = r/r_0$ and $\psi_0 = -v_0 r_0/2a$. For $a = 0.3398$, $b = 5.377 \times 10^{-4}$, $v_0 = 71.521\,\mathrm{ms}^{-1}$ and $r_0 = 100\,\mathrm{km}$ the maximum wind is $40\,\mathrm{ms}^{-1}$ (at $r = r_0$). As for some cases in Ritchie and Holland (1993) and Holland and Dietachmayer (1993) the outer parts of the vortex are characterized by weak negative relative vorticity.

We performed high-resolution reference runs on uniform grids for different initial separations with the non-divergent barotropic model used in Scheck et al. (2011a); Scheck et al. (2011b). In the standard scenario that will be used for adaptive runs later on, we assume an initial cyclone separation distance of $d_i = 400\,\mathrm{km}$, i.e. four times the radius of maximum wind. This separation is too large to allow for a merger, but sufficiently small for the two negative vorticity regions to overlap. In the first 12 hours, in which the vortices perform about a quarter of a full orbit (see Fig. 2), the positive cores are strongly deformed and even connected to each other (at $t = 6\,\mathrm{h}$), but separate again and develop symmetric distributions. During this initial phase, a remarkable change in the distribution of fluid with negative vorticity takes place. The latter is advected towards the regions behind the orbiting positive cores, thereby forming two cyclone-anticyclone pairs. The pairs are oriented such

[1] Bauer et al. (2014) use a shallow-water version of this test case.

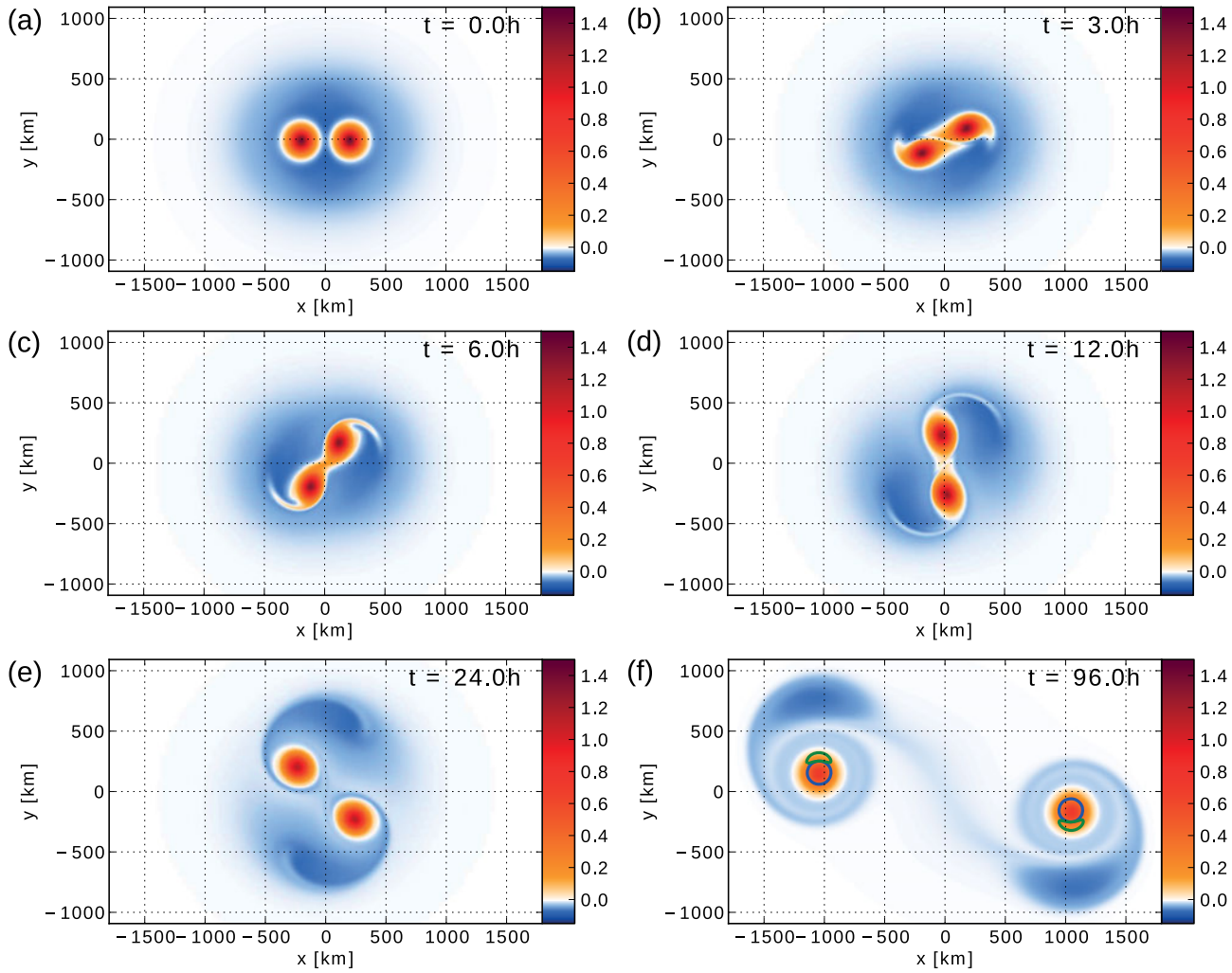

Figure 2: Vorticity distribution for the interaction of two vortices with an initial separation of 400 km at $t = 0$ h, 3 h, 6 h, 12 h, 24 h and 96 h. Vorticity (in colour) is given in units of $10^{-3}s^{-1}$. The blue and green contour lines in the bottom right panel indicate the regions Ω_V and Ω_E, respectively, which are used in the definition of the goal functionals (see Section 2.2).

that they propagate away from each other. Thus the orbiting motion of the positive cores that dominates the dynamics of the initial phase gives way to a linear propagation of the two pairs into opposite directions. After about 48 hours, the mutual influence of the pairs is negligible and they follow straight tracks. This behaviour has also been found in simulations by Valcke and Verron (1997) and is reproduced in laboratory experiments by Beckers et al. (2002).

Further runs for varying initial distance show that the critical cyclone separation below which mergers occur, is about 380 km for this set-up (Fig. 3). Below and close to the critical separation a marked high, nonlinear sensitivity of the solution with respect to the initial state exists. A high sensitivity is also given for initial separations above the critical value. For these cases the time at which the transition from orbiting to straight propagation occurs, depends sensitively on the initial separation and has a large influence on the final cyclone positions. For instance, the cyclones in the run with $d_i = 390$ km orbit each other for about 15 hours longer than in the run with $d_i = 400$ km. Consequently, the

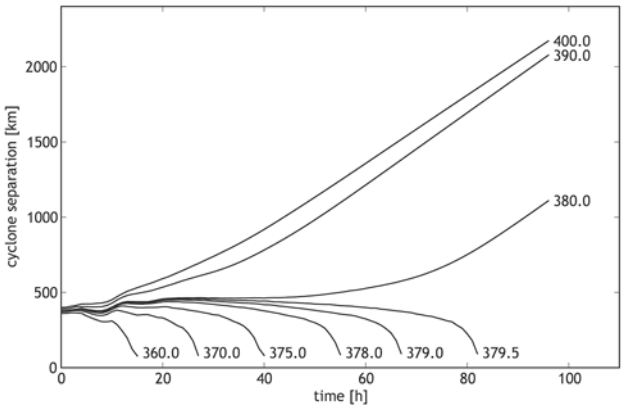

Figure 3: Evolution of the separation of the two storms for several initial separations. The lines end when the separation has become smaller than 100 km. The two storms merge for initial separations smaller that 380 km.

direction of propagation after the orbiting phase differs by about 140 ° for these two cases.

The high sensitivity with respect to perturbations in the initial state suggests that numerical errors, in par-

ticular in the orbiting phase, will have a large influence on the solution. A too coarse grid can even result in a merger of the vortices for initial distances that lead to a separation for higher resolution. The scenario considered here therefore presents a challenging test problem for grid adaptation.

2.2 Goal functionals

The objective of goal-oriented adaptation is the minimization of the discretization error, measured by means of the chosen goal functional. Therefore, the goal functional should represent the most relevant aspects of the results. Tropical cyclone forecasts address several important questions. Where will the cyclone be located? Or, to be more specific, where are the strongest wind speeds to be expected? And how will the intensity of the cyclone develop? The last question cannot be addressed by barotropic models such as the one used in this study. However, we formulated goal functionals related to the first two questions.

The storm centre of an idealized TC located within the domain D can be characterized by the location of the vorticity maximum:

$$J_{\mathrm{Pos}}(\upsilon) := \operatorname*{argmax}_{x\in D}(\nabla \times \upsilon(x)), \tag{2.2}$$

for a fixed velocity field υ. However, J_{Pos} is not a continuous functional, since small perturbations in υ can lead to large changes in $J_{\mathrm{Pos}}(\upsilon)$. Therefore, J_{Pos} cannot be utilized in the DWR framework, where functionals must be three-times differentiable, cf. Bangerth and Rannacher (2003). As an alternative, we propose functionals that are smooth and strongly correlated with the quantities of interest.

For a fixed region Ω_V containing the high-vorticity region near the centre of a cyclone, any displacement of the cyclone will cause the integrated vorticity in Ω_V to change. Therefore, we introduce the following goal functional:

$$J_V(\upsilon) := \int_{\Omega_V} \nabla \times \upsilon(T,x)\,dx, \tag{2.3}$$

where T is the time at the end of the model run. We define Ω_V as the region in which the vorticity at time T is greater than or equal 50 % of the maximum vorticity $\zeta_{\max} := \max_{x\in\Omega}\{\nabla \times \upsilon(T,x)\}$ in the domain, i.e.

$$\Omega_V := \{x \in \Omega \,|\, \nabla \times \upsilon(T,x) \geq 0.5 \cdot \zeta_{\max}\}. \tag{2.4}$$

At the boundary of Ω_V the vorticity gradient is strong and therefore the influence of storm displacements on $J_V(\upsilon)$ can be expected to be strong. During the adaptation cycles of the DWR method, we can determine the high-vorticity region Ω_V based on the solution of the primal problem, which is solved always before the dual problem. However, this means that the goal functional changes from one adaptation cycle to the other.

To investigate the influence of this potential difficulty, we propose a second, similar goal functional, for which the high-vorticity region is assumed to be known in advance and is kept constant during the adaptation cycles. Furthermore, only one of the two storms is considered in the vorticity integration. This set-up corresponds to situations where the position of only one of the storms, e.g. the one about to make landfall, is of particular interest. The two storms thus will not be treated the same way, demonstrating how the goal-oriented approach allows us to focus on the user-specific interests, which would not be possible for alternative grid adaptation methods. The second goal functional is defined as

$$J_{V,\mathrm{ref}}(\upsilon) := \int_{\Omega_{V,\mathrm{ref}}} \nabla \times \upsilon(T,x)\,dx, \tag{2.5}$$

with a circular integration domain around the storm centre of one storm at $P_{\mathrm{ref}} = (-1043.7\,\mathrm{km}, 153.4\,\mathrm{km})$, determined from a high-resolution reference run:

$$\Omega_{V,\mathrm{ref}} := \{x \in \Omega \,|\, \|x - P_{\mathrm{ref}}\|_{l^2} \leq r_{\mathrm{ref}}\}. \tag{2.6}$$

The radius is $r_{\mathrm{ref}} = 93\,\mathrm{km}$ since here the vorticity is approximately 50 % of $\zeta_{\max}$ and therefore $\Omega_{V,\mathrm{ref}}$ corresponds roughly to the sub-domain of Ω_V containing the same storm centre.

Finally, we propose a third goal functional which is related to the area with the highest wind speeds (and thus, the most severe damage to be expected). Using energy instead of vorticity, we define

$$J_E(\upsilon) := \int_{\Omega_E} \|\upsilon(T,x)\|^2\,dx, \tag{2.7}$$

where the domain Ω_E corresponds to the region where the kinetic energy at time T is higher or equal 90 % of the maximum energy $E_{\max} := \max_{x\in\Omega} \|\upsilon(T,x)\|^2$, i.e.

$$\Omega_E := \{x \in \Omega \,|\, \|\upsilon(T,x)\|^2 \geq 0.9 \cdot E_{\max}\}. \tag{2.8}$$

This goal functional is physically as well motivated as J_V, but has the interesting property that it could cause an asymmetry in goal-oriented adapted grids. On the right side of the track of a moving TC on the northern hemisphere the absolute wind speeds are higher, because the translation velocity and the storm circulation have the same direction. For the definition given above, Ω_E will be dominated by the flow on the right of the storm. In contrast, Ω_V is symmetric and centred on the vorticity maximum. Asymmetries in the structure of TCs are known to have a potentially large impact on their development. The motivation to consider J_E is therefore to test, whether the artificial asymmetry introduced by grid adaptation has an influence on the quality of the solution.

3 Model equations and discretization

In this section, we introduce the equations of the model used to describe the dynamics of the cyclone scenario

(denoted *primal problem*) and the corresponding linearized adjoint problem (denoted *dual problem*) based on which the goal functional's sensitivity can be determined. For these two models we present variational formulations defined on continuous function spaces and describe the space-time finite element discretization used later. We consider the variational formulations, since the goal-oriented error estimator (see Section 4) is defined in terms of this formulation.

3.1 Primal and dual problem

For the discretization of the scenario described in Section 2.1, we use a non-divergent barotropic model. This widely-used idealization assumes that velocity does not depend on height and corresponds to the two-dimensional incompressible Navier-Stokes equations.

We consider the domain $\Omega := [-L_1, L_1] \times [-L_2, L_2]$, where $L_1 = 2000\,\text{km}$ and $L_2 = 1732\,\text{km}$ and regard the time horizon $[0, T]$ with $T = 96\,\text{h}$. The solution variables are the velocity field $v : [0, T] \times \Omega \to \mathbb{R}^2$ and the pressure field $p : [0, T] \times \Omega \to \mathbb{R}$. The dynamics of the atmosphere is described by the incompressible Navier-Stokes equations

$$\begin{cases} \partial_t v + (v \cdot \nabla)v - \nu \Delta v + \nabla p &= 0, \\ \nabla \cdot v &= 0, \\ v_{|t=0} &= v_0, \end{cases} \tag{3.1}$$

where the initial velocity field v_0 is defined such that two vortices with initial separation $d_i = 400\,\text{km}$ as described in Section 2.1 exist. A kinematic viscosity value of $\nu = 0.005\,\text{km}^2\text{s}^{-1}$ was chosen, which is sufficiently high to suppress numerical noise and not too high to lead to an excessive damping of the vortices during the considered time interval. We use a space-periodic domain where velocity and pressure fulfil

$$\begin{aligned} v(t, x + L_i e_i) &= v(t, x - L_i e_i), \\ p(t, x + L_i e_i) &= p(t, x - L_i e_i), \end{aligned} \tag{3.2}$$

for $i \in \{1, 2\}$, $(t, x) \in [0, T] \times \Omega$ and e_i denoting Cartesian unit vectors.

In the following, variational formulations of the problem (3.1) and the corresponding dual problem are presented. The definitions of the function spaces X, Y, and M and the $(\cdot, \cdot)$-notation are given in the appendix.

The continuous primal problem

Find $(v, p) \in X \times M$ such that

$$\rho(v, p)(\varphi, \psi) = 0 \tag{3.3}$$

for all $(\varphi, \psi) \in Y \times M$, where the residual operator of the primal problem is defined by

$$\begin{aligned} \rho(v, p)(\varphi, \psi) := \int_0^T \Big(&(\partial_t v + (v \cdot \nabla)v, \varphi) \\ &+ \nu(\nabla v, \nabla \varphi) - (p, \nabla \cdot \varphi) \\ &+ (\nabla \cdot v, \psi) \Big)\, dt \\ &+ (v_{|t=0} - v_0, \varphi_{|t=0}). \end{aligned}$$

The continuous dual problem

The dual problem associated to (3.3) can be derived for a user-defined goal functional $J : Y \to \mathbb{R}$ by the method of Lagrange multipliers[2]. It is defined by means of the adjoint of the primal problem's linearised operator and is posed backward in time: Find $(z, q) \in X \times M$ such that

$$\rho^*(z, q)(\varphi, \psi) = 0 \tag{3.4}$$

for all functions $(\varphi, \psi) \in Y \times M$. The residual of the dual problem is defined as

$$\begin{aligned} \rho^*(z, q)(\varphi, \psi) := \int_0^T \Big(&- (\partial_t z, \varphi) + \nu(\nabla \varphi, \nabla z) \\ &+ ((v \cdot \nabla)\varphi + (\varphi \cdot \nabla)v, z) \\ &- (\nabla \cdot z, \psi) + (\nabla \cdot \varphi, q) \Big)\, dt \\ &+ (z_{|t=T}, \varphi_{|t=T}) + \nabla J(u)\varphi. \end{aligned}$$

3.2 Space-time finite element discretization

For the discretization in space, we consider a triangulation $\mathcal{T}_h$ of the domain Ω consisting of quadrilaterals and introduce piecewise bi-quadratic functions for the velocity and piecewise bi-linear functions for the pressure variable, both globally continuous. It is well-known, that these so-called Taylor-Hood elements fulfil the Brezzi condition, Brezzi (1974), and are stable, Brezzi and Falk (1991). The discrete velocity space is denoted $V_h \subseteq V$ and the discrete pressure space $Q_h \subseteq Q$ (see appendix for details).

For the discretization in time, a finite element method called cGP(1), Schieweck (2010), is utilized which makes use of test functions that may be discontinuous in the time dimension. By means of the discontinuities, discrete solutions can be determined iteratively by stepping through subintervals of the time horizon. In contrast to many other time-stepping schemes, the cGP(1) method provides a Galerkin property related to the time discretization which allows for an a posteriori error estimation based on the DWR method also in time. For a partitioning $0 = t_0 < t_1 < \ldots < t_N = T$ the trial and test functions are defined as piecewise polynomials in

[2] The goal functionals introduced in Section 2.2 fit into this frame and can be written as $J(v) = (j, v(T))$ for some $j \in L^2(\Omega)^2$ by a L^2-projection. Their linearisation is $\nabla J(v)\varphi = (j, \varphi_{|t=T})$ and therefore j plays the role of the dual problem's initial state posed at the model run's end time: $z_{|t=T} = j$.

time (see appendix for the precise definition of the subsequently used $\mathbb{P}$-notation). For the velocity ansatz functions, we introduce the space $X_{\tau h} = \mathbb{P}_1^c(V_h)$ of piecewise linear, globally continuous functions. The velocity test functions are piecewise constant (corresponding space denoted $Y_{\tau h} = \mathbb{P}_0^{dc}(V_h)$). For the pressure variable, test and trial functions are piece-wise constant and elements of the space $M_{\tau h} = \mathbb{P}_0^{dc}(Q_h)$. The spaces $Y_{\tau h}$ and $M_{\tau h}$ allow for discontinuous only at the points in time t_i.

The discrete versions of the primal and dual problem discussed in the following are formulated in terms of these discrete function spaces.

The discrete primal problem

The solution of the discrete primal problem is the tuple $(\upsilon_{\tau h}, p_{\tau h}) \in X_{\tau h} \times M_{\tau h}$ that fulfils

$$\rho(\upsilon_{\tau h}, p_{\tau h})(\varphi, \psi) = 0, \tag{3.5}$$

for all $(\varphi, \psi) \in Y_{\tau h} \times M_{\tau h}$. The operator ρ is defined as for problem (3.3).

The discrete dual problem

The solution of the discrete dual problem is the tuple $(z_{\tau h}, q_{\tau h}) \in X_{\tau h} \times M_{\tau h}$ that fulfils

$$\rho^*(z_{\tau h}, q_{\tau h})(\varphi, \psi) = 0, \tag{3.6}$$

for all $(\varphi, \psi) \in Y_{\tau h} \times M_{\tau h}$. The operator ρ^* is defined as for problem (3.4).

4 Error estimation and adaptation strategy

In this section, we formulate the estimator for the error in goal functionals and describe the utilized adaptation strategy based on corresponding error indicators. An extension of the concepts described in Bangerth and Rannacher (2003) is needed to enable adaptivity of the time discretization, similarly to Schmich and Vexler (2007). We present a tailored variant which is adequate for Petrov-Galerkin approximations as the one described in Section 3.2. We provide detailed descriptions of the applied error characterization variant and the corresponding cell-wise error indicators which can easily be computed. Finally, we describe the adaptation strategies that are used to construct spatial meshes and time partitionings based on the goal-oriented error indicators.

4.1 A posteriori error characterization

The goal-oriented error characterization of the primal problem's solution is based on an abstract error characterization described in the following. For better readability, we introduce the notations $W := X \times M$ and $L := Y \times M$. A variational form of the primal problem and the dual problem (assuming a three times differentiable functional $J : W \to \mathbb{R}$) is given by: Find $u, \lambda \in W$ such that

$$\begin{aligned} \rho(u)(\varphi) &= 0, \\ \rho^*(\lambda)(\varphi) := \nabla_u \rho(u)(\lambda)\varphi &= J'(u)\varphi, \end{aligned} \tag{4.1}$$

for any $\varphi \in L$. The Petrov-Galerkin approximations $u_{\tau h}, \lambda_{\tau h} \in W_{\tau h}$ are solutions of the discrete version of problem (4.1), where the spaces W and L are replaced by discrete counterparts $W_{\tau h} \subset W$ and $L_{\tau h} \subset L$. The following characterization of the error in J holds:

$$\begin{aligned} J(u) - J(u_{\tau h}) = &\frac{1}{2}\Big(\rho(u_{\tau h})(\lambda + \lambda_{\tau h} - \varphi_{\tau h}) \\ &+\rho^*(\lambda_{\tau h})(u - u_{\tau h} - \psi_{\tau h})\Big) + \mathcal{R}, \end{aligned} \tag{4.2}$$

with arbitrary $\varphi_{\tau h}, \psi_{\tau h} \in L_{\tau h}$ and remainder $\mathcal{R}$ which is of third order in the error $u - u_{\tau h}$ and $\lambda - \lambda_{\tau h}$. A proof can be found in Baumann (2011). Note that the discrete solutions $u_{\tau h}, \lambda_{\tau h} \in W_{\tau h}$ are not included in the function space $L_{\tau h}$ in general. The error characterization (4.2) is given in terms of the unknown quantities u, λ, and $\mathcal{R}$. It is common practice to neglect the remainder $\mathcal{R}$ and to replace the unknown solutions u and λ by approximations to obtain a version that can easily be computed, see e.g. Bangerth and Rannacher (2003). We make use of higher-order patch-interpolation in space and nodal interpolation in time to determine approximations. For the separation of the discretization error in space and time, we introduce two estimators $E^{(\text{time})}$ and $E^{(\text{space})}$, as proposed by Schmich and Vexler (2007)[3].

In space, we consider the space $\hat{V}_h \times \hat{Q}_h$ consisting of higher-order Taylor-Hood elements Q_4/Q_2. The combination of Q_2/Q_1 and Q_4/Q_2 allows a straightforward interpretation of a patch of Q_2/Q_1-cells as one larger Q_4/Q_2-cell as described e.g. in Bangerth and Rannacher (2003), see Fig. 4(a). We denote the corresponding higher-order patch interpolator by

$$\hat{I}_{2h} : (V_h \times Q_h) \to (\hat{V}_h \times \hat{Q}_h).$$

In the time dimension we introduce a higher-order space only for the pressure. The piecewise constant pressure functions are transformed into a piecewise linear and globally continuous function by nodal interpolation:

$$\hat{I}_\tau : (\mathbb{P}_1^c(\hat{V}_h) \times \mathbb{P}_0^{dc}(\hat{Q}_h)) \to (\mathbb{P}_1^c(\hat{V}_h) \times \mathbb{P}_1^c(\hat{Q}_h)),$$

see Fig. 4(b). With these interpolations, efficient higher-order representations of the discrete solutions of the primal and dual problem can be defined by

$$\begin{aligned} (\hat{\upsilon}, \hat{p}) &:= \hat{I}_\tau(\hat{I}_{2h}(\upsilon_{\tau h}, p_{\tau h})), \\ (\hat{z}, \hat{q}) &:= \hat{I}_\tau(\hat{I}_{2h}(z_{\tau h}, q_{\tau h})), \end{aligned}$$

which will be inserted as test functions in the primal and dual residual for error estimation. It is well-known

[3]This approach assumes that the discrete residual operator are good approximations of the time-discrete operators, i.e. $\rho(u_{\tau h})(\cdot) \approx \rho(u_\tau)(\cdot)$ and $\rho(\lambda_{\tau h})(\cdot) \approx \rho(\lambda_\tau)(\cdot)$.

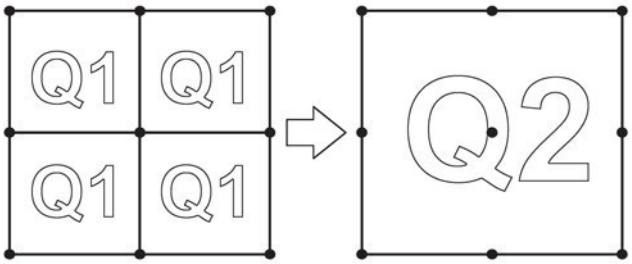

(a) Patch of four cells forming one bigger cell with higher finite element ansatz. The nodal points of the respective Lagrange finite elements are located at the same places.

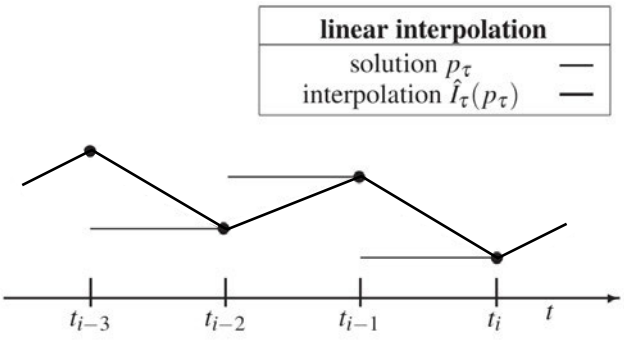

(b) Piecewise linear interpolation of a piecewise constant function.

Figure 4: Higher-order interpolation in two space dimensions (a) and in the time dimension (b). Dots represent nodal points of the respective finite elements.

that the residual of a Galerkin solution vanishes for all test functions of the test space associated to the discrete problem. This so-called *Galerkin orthogonality* guarantees that the residual remains unchanged when arbitrary discrete functions are added to the test functions. Hence, the discrete parts of the higher-order primal and dual solutions may be subtracted before using them as test functions during the error estimation which is beneficial when cell-wise contributions are determined. For the identification of the discrete parts, we introduce the nodal interpolations

$$I_h : (\hat{V}_h \times \hat{Q}_h) \to (V_h \times Q_h),$$
$$I_\tau : (\mathbb{P}_1^c(\hat{V}_h) \times \mathbb{P}_1^c(\hat{Q}_h)) \to (\mathbb{P}_1^c(\hat{V}_h) \times \mathbb{P}_0^{dc}(\hat{Q}_h)).$$

Finally, we define the approximations of the time-discrete solutions of the primal and dual problem by

$$(\hat{v}_\tau, \hat{p}_\tau) := I_\tau(\hat{v}, \hat{p}),\ (\hat{z}_\tau, \hat{q}_\tau) := I_\tau(\hat{z}, \hat{q}).$$

With these notations, the error characterization related to the time discretization can be stated as

$$E^{(\text{time})} = \rho(v_{\tau h}, p_{\tau h})(Z^{(\text{time})}, Q^{(\text{time})}), \tag{4.3}$$

which can be computed easily since all quantities are known, i.e.

$$(Z^{(\text{time})}, Q^{(\text{time})}) := (\hat{z}_\tau, \hat{q}_\tau) - I_\tau(\hat{z}_\tau, \hat{q}_\tau).$$

The error characterization related to the space discretization can be stated as

$$E^{(\text{space})} = \frac{1}{2}\Big[\rho(v_{\tau h}, p_{\tau h})(Z^{(\text{space})}, Q^{(\text{space})}) + \rho^*_{u_{\tau h}}(z_{\tau h}, q_{\tau h})(U^{(\text{space})}, P^{(\text{space})})\Big], \tag{4.4}$$

with computable representations

$$(Z^{(\text{space})}, Q^{(\text{space})}) := (\hat{z}_\tau + z_{\tau h}, \hat{q}_\tau + q_{\tau h}) - I_h(\hat{z}_\tau + z_{\tau h}, \hat{q}_\tau + q_{\tau h}),$$
$$(U^{(\text{space})}, P^{(\text{space})}) := (\hat{v}_\tau - v_{\tau h}, \hat{p}_\tau - p_{\tau h}) - I_h(\hat{v}_\tau - v_{\tau h}, \hat{p}_\tau - p_{\tau h}).$$

4.2 Error indicators

From the error characterizations (4.3) and (4.4) we derive cell-wise error indicators for the control of subsequent adaptation. To this end, the primal and dual residual functionals ρ and ρ^* are rewritten as sums of integrals over cells in the space-time mesh where parts related to the initial conditions are neglected for simplicity. Assuming a time-independent mesh $\mathcal{T}_h$ and N_{time} time intervals, the residual of the discrete primal problem (3.5) has the form

$$\rho(v_{\tau h}, p_{\tau h})(Z, Q) := \sum_{i=1}^{N_{\text{time}}} \sum_{K \in \mathcal{T}_h} \rho_{K,i}(Z, Q),$$

with contributions

$$\rho_{K,i}(Z, Q) := \int_{t_{i-1}}^{t_i} \big((\partial_t v_{\tau h} + (v_{\tau h} \cdot \nabla) v_{\tau h}, Z)_K + \nu(\nabla v_{\tau h}, \nabla Z)_K - (p_{\tau h}, \nabla \cdot Z)_K + (\nabla \cdot v_{\tau h}, Q)_K\big)\, dt, \tag{4.5}$$

where $(\cdot,\cdot)_K$ denotes an integral over the cell K. Since $\rho_{K,i}(Z, Q)$ is defined on single cells and therefore all appearing functions are polynomials, integration by parts can be applied leading to additional integrals over cell edges. Each cell's contribution results in

$$\tilde{\rho}_{K,i}(Z, Q) := \int_{t_{i-1}}^{t_i} \big((R, Z)_K + (\nabla \cdot v_{\tau h}, Q)_K + (r, Z)_{\partial K}\big)\, dt, \tag{4.6}$$

where the *cell-residual* R is defined as

$$R := \partial_t v_{\tau h} + (v_{\tau h} \cdot \nabla) v_{\tau h} + \nabla p_{\tau h} - \nu \Delta v_{\tau h} \tag{4.7}$$

and $(\cdot,\cdot)_{\partial K}$ denotes an integral along the cell's edge. The *edge residual* r represents contributions over the common edge $\gamma := \partial K' \cap \partial \hat{K}$ of two neighbouring cells $K', \hat{K} \in \mathcal{T}_h$. Their contributions are accumulated resulting in the jump of the derivatives over the common edge. Denoting $(\cdot)'$ and $\hat{(\cdot)}$ the contributions of $(\cdot)$ on

the cells K' and $\hat{K}$, respectively, the contribution of both cells is

$$\begin{aligned}&(\nu\partial_{n'}v'_{\tau h} - p'_{\tau h}n', Z')_\gamma + (\nu\partial_{\hat{n}}\hat{v}_{\tau h} - \hat{p}_{\tau h}\hat{n}, \hat{Z})_\gamma \\ &= \nu(\partial_n v'_{\tau h} - \partial_n \hat{v}_{\tau h}, Z)_\gamma,\end{aligned} \tag{4.8}$$

where the fact that the dual velocity Z and the primal pressure $p_{\tau h}$ are globally continuous and the normal unit vectors of the two cells are anti-parallel (i.e. $n := n' = -\hat{n}$) was exploited. Hence, the edge residual is defined as

$$r := \begin{cases} \frac{1}{2}\nu(\partial_n v'_{\tau h} - \partial_n \hat{v}_{\tau h}), & \text{if } \gamma \not\subseteq \partial\Omega, \\ \nu\partial_n v_{\tau h} - p_{\tau h}n, & \text{if } \gamma \subseteq \partial\Omega. \end{cases}$$

In similar way, the residual of the discrete dual problem $\rho^*_{v_h}(z_{\tau h}, q_{\tau h})(U, P)$ can be written as sum of cell contributions. Using integration by parts,

$$\begin{aligned}\tilde{\rho}^*_{K,i}(U, P) := \int_{t_{i-1}}^{t_i} \Big(&(R^*, U)_K - (\nabla \cdot z_{\tau h}, P)_K \\ &+ (r^*, U)_{\partial K} \Big) dt,\end{aligned} \tag{4.9}$$

where the dual problem's cell residual R^* and edge residual r^* have the form

$$\begin{aligned}R^* :=& -\partial_t z_{\tau h} + ((\nabla v_{\tau h})^T - (\nabla \cdot v_{\tau h}) \\ &- (v_{\tau h} \cdot \nabla))\, z_{\tau h} - \nu\Delta z_{\tau h} - \nabla q_{\tau h}, \\ r^* :=& \begin{cases} \frac{1}{2}\nu(\partial_n z'_{\tau h} - \partial_n \hat{z}_{\tau h}), & \text{if } \gamma \not\subseteq \partial\Omega, \\ (v_{\tau h} \cdot n) z_{\tau h} + \nu\partial_n z_{\tau h} + q_{\tau h}n, & \text{if } \gamma \subseteq \partial\Omega. \end{cases}\end{aligned}$$

Cell-wise error indicators for the temporal error contributions are defined by

$$\eta^{(\text{time})}_{K,i} := |\tilde{\rho}_{K,i}(Z^{(\text{time})}, Q^{(\text{time})})| \tag{4.10}$$

and the spatial indicators are defined by

$$\begin{aligned}\eta^{(\text{space})}_{K,i} := \frac{1}{2}|&\tilde{\rho}_{K,i}(Z^{(\text{space})}, Q^{(\text{space})}) \\ &+ \tilde{\rho}^*_{K,i}(U^{(\text{space})}, P^{(\text{space})})|.\end{aligned} \tag{4.11}$$

These indicators contain information about the origin of errors and can be used to control the adaptation of the discretization in different ways, e.g. local mesh refinement, nesting, and adaptive time-stepping.

4.3 Adaptation strategy

We consider a restricted form of adaptivity where the space dimension is decoupled from the time dimension. In the following, we derive reduced error indicators (due to the separation of space and time dimension) and describe the iterative adaptation strategies by which the spatial error indicators should be balanced over the mesh and the temporal error indicators over the partition[4].

Adaptation of the space discretization

For the steering of the mesh, we introduce a reduced form of spatial indicators by taking the maximum error indication of each cell over all time intervals:

$$\eta^{(\text{space})}_K := \max_{j=0}^{N_{\text{time}}} \eta^{(\text{space})}_{K,j}, \tag{4.12}$$

for any cell $K \in \mathcal{T}_h$. With regard to the comparison of optimized meshes based on different goal functionals, an adaptation strategy is desired that leads to meshes with a given number of cells. During the mesh adaptation, the periodicity of the domain must be considered (see condition (3.2)), the mesh should fulfil the *1-irregularity* condition[5], and a patch-structure is required (for efficient computation of the higher-order interpolation, see Fig. 4(a)). These requirements make the adaptation towards a mesh with given number of cells a non-trivial task, since each cell-refinement can imply the refinement of several other cells on one hand and cells that are marked to be coarsened will only be coarsened if all involved cells are also marked on the other hand. Therefore, we apply an iterative mesh adaptation procedure and decouple the steps of coarsening and refinement.

Assume that a mesh consisting of $N^{(\text{opt})}_{\text{space}}$ cells should be constructed with balanced error indicators. In the ith adaptation cycle of the DWR method, let the current mesh consists of N^i_{space} cells. Then the objective in the current adaptation step is a mesh consisting of

$$N^{(\text{opt}),i+1}_{\text{space}} := N^i_{\text{space}} + k(N^{(\text{opt})}_{\text{space}} - N^i_{\text{space}}),$$

cells, where $k \in (0, 1]$ is a damping parameter (we used $k = 0.7$). We assume that refining a cell into four smaller cells (for quadrilaterals) results in a reduction of the error for the covered area by a factor of $(1/2)^\alpha$. The parameter $\alpha > 0$ describes the order of the reduction (we used $\alpha = 2$). A cell is marked to be coarsened, if its indicated error is smaller than the coarsening bound of

$$B_c := \eta_{\text{avg}}(1/2)^{\alpha+2},$$

where η_{avg} is the desired average value, defined as the sum of the indicators divided by $N^{(\text{opt}),i+1}_{\text{space}}$. The factor $(1/2)^\alpha$ corresponds to error reduction in case of refinement and $(1/2)^2$ accounts for the increased number of cells (one cell is refined into four). Hence, cells are marked to be coarsened only if the expected error is η_{avg} at most. The coarsening of all marked cells results in a mesh with $\bar{N}^i_{\text{space}}$ cells. If $\bar{N}^i_{\text{space}} < N^{(\text{opt}),i+1}_{\text{space}}$, we apply an iteration of successive mesh refinements. In each step, a small number of cells with highest error indicators is refined (only cells are allowed that existed in the mesh on which the error indicators where calculated). If the

[4] It has been described in literature for the case of global error norms that an optimal mesh can be characterized by an equilibrium of local error contributions, see e.g. Babuška and Rheinboldt (1978); Eriksson and Johnson (1991).

[5] At most one inner nodal point (i.e. hanging node) of any neighbouring cell may exist on any edge of any cell in the mesh. This condition reduces the implementation complexity for global continuity of solutions and reduces the number of constrained degrees of freedom at hanging nodes.

resulting mesh contains $N_{\text{space}}^{(\text{opt}),i+1}$ cells (with an accuracy of 5 %), the refinement iteration stops and the mesh is accepted for the next DWR cycle.

The iteration over DWR cycles terminates, if the previously described strategy causes no more coarsening or refining, which means that the error indicators are well-balanced. The desired number of cells is approximately achieved (often up to an accuracy of few cells) as long as enough DWR cycles have been performed. For the adaptive runs of the tropical cyclone scenario, we discuss the number of cells of the meshes during the DWR cycles in the last paragraph of Section 6.1.

Adaptation of the time discretization

We seek a partition of the time interval with a given number of sub-intervals for which the corresponding temporal error indicators are well-balanced. To control the adaptation, we introduce a reduced error indicator for each sub-interval corresponding to the maximum indicator over all cells of the mesh. On the jth time-interval, the indicator is defined by

$$\eta_j^{(\text{time})} := \max_{K\in\mathcal{T}_h(j)} \eta_{K,j}^{(\text{time})}, \tag{4.13}$$

assuming a partition $t_0 < \cdots < t_{N_{\text{time}}}$. To deduce an optimal partition based on the error indicators, the following relation between error indicator and time step $\Delta t_j = t_j - t_{j-1}$ is assumed for any $j \in \{1,\dots,N_{\text{time}}^k\}$:

$$\eta_j^{(\text{time})} = C_j \cdot (\Delta t_j)^\beta. \tag{4.14}$$

Here, $\beta > 0$ is a parameter that describes the order of the error that we introduce as a constant over the interval $[0,T]$ (we used $\beta = 2$). This relation can be stated in terms of a piecewise constant function

$$C(t) := \eta_j^{(\text{time})}/\Delta t_j^\beta, \quad t \in [t_{j-1}, t_j). \tag{4.15}$$

The conditions for the optimal partition can be formulated by means of $D : [0,T] \to \mathbb{R}$ and $E : [0,T] \to \mathbb{R}$ representing the time-step sizes and the error indication as functions in time. The optimal partitioning should consist of $N_{\text{time}}^{(\text{opt})}$ cells, which can be stated as

$$\int_0^T 1/D(t)\,dt = N_{\text{time}}^{(\text{opt})}. \tag{4.16}$$

The error indicators of all sub-intervals should be approximately at the same level, denoted by a constant $\bar{E} \in \mathbb{R}$.

$$E(t) \equiv \bar{E}. \tag{4.17}$$

Assuming that relation (4.15) holds also for the optimal partition results in $C(t) = \bar{E}/D(t)^\beta$. By equation (4.16), the constant indicator $\bar{E}$ can be determined by

$$\bar{E} = \left(\int_0^T C(t)^{1/\beta} dt / N_{\text{time}}^{(\text{opt})}\right)^\beta$$

and D has the form

$$D(t) = (C(t)/\bar{E})^{1/\beta}.$$

The optimized partition can be constructed successively in terms of function D: Let $t_0 := 0$ and for each $j \in \{1,\dots,N_{\text{time}}^{(\text{opt})}\}$ let the point in time t_j be defined such that $\int_{t_{j-1}}^{t_j} D(t)\,dt = 1$. We implemented this procedure approximately with a sampling rate of one second for the TC scenario in which $T = 96$ h.

Parameters of the adaptation strategy

For the adaptation strategy three parameters α, β, and k, are used. Since these parameters are not used in the definition of the error estimator or in the stopping criterion of the iterative adaptation procedure, these parameters have no direct influence on the optimized mesh or the optimized partition of the time-interval in case of convergence of the iteration.

However, the parameters can have strong influence on the convergence properties of the adaptive procedure in general. The parameters α and β represent an (assumed) convergence rate characterizing the relation between local error indicator and local discretization parameter h or Δt. This relation is exploited to derive guesses for optimal discretizations in space and time. For the goal functionals J_V, $J_{V,\text{ref}}$, and J_E the convergence rate however is not known. Noting that these functionals are defined in terms of integrals over the squared velocity and first-order derivatives, there is a relation to localized versions of the global H^1-norm for which the convergence rate of the discrete method is known to be 2, cf. Brezzi and Falk (1991). For the cGP(1) method applied for the time-discretization, the convergence rate is also 2, cf Schieweck (2010). Therefore, we chose the two parameters as $\alpha = \beta = 2$ and observed in numerical tests that small variances have small influence on the convergence property of the over-all adaptation procedure for this scenario.

The parameter $k \in (0,1]$ is introduced as a damping parameter for the desired number of cells in each adaptation cycle. Values $k < 1$ can lead to an increase in the number of required adaptation cycles. This can be favorable in cases where the sensitivity and the corresponding error estimates were not very accurate due to large approximation errors (e.g. first adaptation cycles on very coarse meshes). As long as k is not too small, the number of iterations is not increased significantly.

5 Interpretation of the dual solution

In this section, we first give a general, physical interpretation of the dual solution by revealing how it is connected to sensitivity measures used in meteorology. Subsequently, we discuss the structure of the dual solution for the binary cyclone problem.

5.1 Relation to meteorological sensitivity measures

The dual solution as sensitivity

We investigate the influence that perturbations have on a goal functional based on a formulation that takes perturbations into account. For simplicity, we neglect the constraint of the velocity field being divergence-free and consider an abstract variational problem in terms of the residual operator $\rho : V \to V^*$ where V^* denotes the space of linear and continuous functions that map functions of the Hilbert space V on $\mathbb{R}$. The unperturbed problem has the form:

$$\upsilon \in V : \quad \rho(\upsilon)(\varphi) = 0 \quad \forall \varphi \in V. \tag{5.1}$$

The influence of a perturbations $p \in V$ can be considered by including $P(p)(\varphi) := (p, \varphi)$ to problem (5.1). The solution $\upsilon \in V$ of the perturbed problem must fulfill

$$\tilde{\rho}(\upsilon, p)(\varphi) := \rho(\upsilon)(\varphi) + P(p)(\varphi) = 0, \tag{5.2}$$

for all $\varphi \in V$.

By the implicit functional theorem applied to (5.2), $\upsilon = \upsilon(p)$ is continuously differentiable and it holds in the sense of V^* (see e.g. Hinze et al. (2008)):

$$\begin{aligned} 0 &= \frac{\partial}{\partial \upsilon}\rho(\upsilon(p))\upsilon'(p) + P'(p) \\ \Leftrightarrow \quad \upsilon'(p) &= -\left[\frac{\partial}{\partial \upsilon}\rho(\upsilon(p))\right]^{-1} Id_V. \end{aligned} \tag{5.3}$$

A functional's sensitivity S on some perturbation δ is given by means of its directional derivative:

$$\begin{aligned} \langle S, \delta\rangle :&= \frac{d}{dp}J(\upsilon(p)) \cdot \delta = \langle J'(\upsilon), \upsilon'(p) \cdot \delta\rangle \\ &= \left\langle [\upsilon'(p)]^* J'(\upsilon), \delta \right\rangle \\ &\overset{(5.3)}{=} \left\langle -\left(\left[\frac{\partial}{\partial \upsilon}\rho(\upsilon)\right]^{-1}\right)^* J'(\upsilon), \delta \right\rangle. \end{aligned} \tag{5.4}$$

The dual problem to (5.2) seeks for $z \in V$ such that

$$\begin{aligned} \rho^*(z)(\varphi) :&= \langle \rho'(\upsilon)\varphi, z\rangle + J'(\upsilon)\varphi \\ &= \left\langle [\rho'(\upsilon)]^* z, \varphi \right\rangle + J'(\upsilon)\varphi = 0, \end{aligned} \tag{5.5}$$

for all $\varphi \in V$. By means of the solution z, the influence of a perturbation δ can be written as

$$\langle S, \delta\rangle = \left\langle -\left([\rho'(\upsilon)]^{-1}\right)^* J'(\upsilon), \delta \right\rangle = \langle z, \delta\rangle . \tag{5.6}$$

Hence, the sensitivity S corresponds to the dual solution. For many meteorological applications, the investigation of perturbed initial conditions is very important. In this case, the scalar product in (5.6) has only a contribution at initial time $t = 0$, i.e. $\langle S, \delta_0\rangle = \langle z(0), \delta_0\rangle$. This quantity corresponds to the first-order approximation described in equation(4) on page 2579 of Errico (1997). The adjoint of the model used in this approximation and the dual solution described in our article are based on the same mathematical concept. However, the numerical approaches used to determine the two quantities are quite different. We introduced the dual problem in a functional analytic frame since the error estimation is defined in terms of a continuous dual residual operator. The dual problem is discretised afterwards to calculate approximate solutions. In contrast, in meteorological model systems adjoint sensitivity is often calculated by generating an adjoint version of the discretised equations, often using tools automating this process (see e.g. Giering and Kaminski (1998)). Numerically the dual solution and the adjoint sensitivity thus are not guaranteed to be identical.

The dual solution as optimal perturbation

The adjoint sensitivity can also be considered as an optimal perturbation. Of all initial perturbations causing a given change $\delta_J \in \mathbb{R}$ in the goal functional J they have the smallest norm. The dual solution is related to the same optimization problem, but the underlying norm is not restricted to the time $t = 0$. The optimal perturbations are solution of:

$$\min_{\delta \in V} \|\delta\|^2, \quad \text{constraint: } \frac{d}{dp}J(\upsilon(p)) \cdot \delta = \delta_J, \tag{5.7}$$

where we assume that the norm is defined in terms of a scalar product $\|\delta\| := \sqrt{\langle \delta, \delta\rangle}$. A corresponding Lagrange functional has the form

$$\mathcal{L}(\delta, \lambda) = \langle \delta, \delta\rangle + \lambda(\delta_J - \langle S, \delta\rangle). \tag{5.8}$$

By relation (5.6), it holds $\langle S, \delta\rangle = \langle z, \delta\rangle$. An extremum of (5.8) must fulfill the necessary condition

$$\frac{\partial}{\partial \delta}\mathcal{L}(\delta, \lambda)\varphi = 2\langle \delta, \varphi\rangle - \lambda\langle z, \varphi\rangle = 0, \tag{5.9}$$

for all $\varphi \in V$. Therefore, the optimal perturbation is a scaled dual solution, i.e. $\delta \propto z$. Restricting the allowed perturbations to the initial state at $t = 0$, the optimal perturbation is a scaled version of the dual solution at $t = 0$, i.e. $\delta_0 \propto z(0)$.

The singular vector approach is used in meteorology, in addition to the adjoint sensitivity, to create optimal perturbations which are also used to quantify sensitivity and determine sensitive regions. Singular vectors are solutions to a different optimization problem. They are the perturbations showing the strongest growth, e.g. in the energy norm, for a given time interval (see Scheck et al. (2013)). Despite the differing optimization problems in case of adjoint sensitivity and singular vectors, their structures can be quite similar, as we will show in the next section.

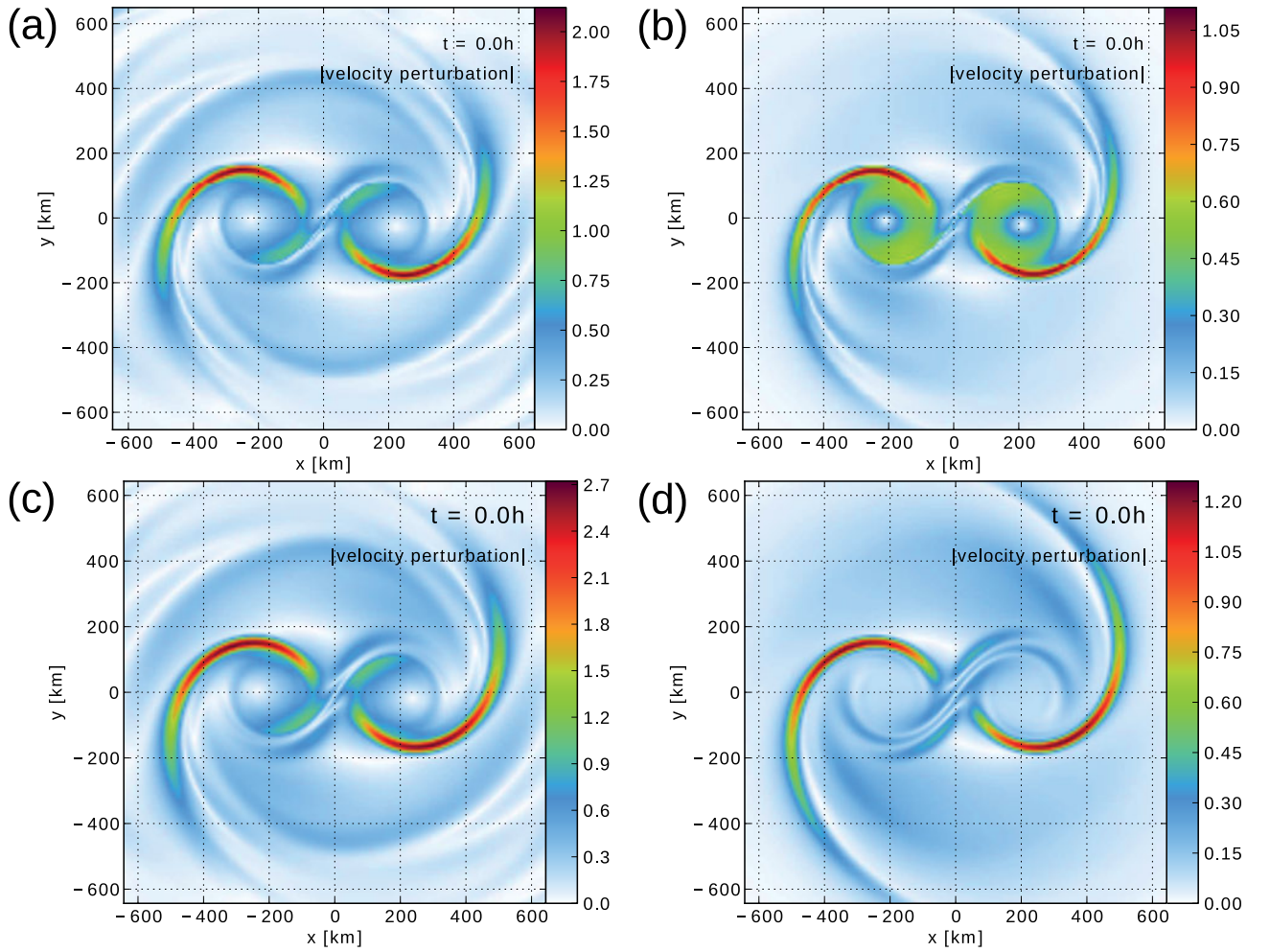

Figure 5: Absolute value of the dual velocity at $t = 0$ for (a) the J_E and (b) the J_V goal functional computed with HiFlow^3 and (c) again for J_E, but computed with the finite difference code of Scheck et al. (2013), which was also used to compute (d) the leading singular vector for the energy norm. All quantities are scaled such that their integrated perturbation energy in $r < 1000$ km is the same.

5.2 Structure of the dual solution for binary vortex interaction

The distributions of the dual velocity for the goal functionals J_V and J_E at $t = 0$ (Fig. 5(a,b)) are quite similar. Both are dominated by thin filaments located north-west of the western and south-east of the eastern vortex, at distances between 150 km and 300 km. For J_E more structure is visible at larger radii, and for J_V somewhat higher sensitivity is found closer to the vortex centres, but the dominant structures are nearly identical. For comparison, we computed the adjoint sensitivity for J_E (Fig. 5(c)) and the leading energy singular vector (Fig. 5(d)) using the finite difference code described in Scheck et al. (2013). The adjoint sensitivity is nearly identical to the dual solution, indicating that in both cases physical processes and not numerical effects determine these quantities. The same dominant structures as in the dual solutions are also found in the leading singular vector, although the latter is the solution of a different optimization problem.

All of these optimal perturbations have the same effect – they cause a displacement of the vortices in the final state. As an example, the linear time evolution of a vorticity perturbation that is initially proportional to the adjoint sensitivity for J_E (Fig. 5(c)) is shown in Fig. 6. The thin vorticity filaments are initially tilted against the shear (Fig. 6(a)). The shear flow "untilts" these structures, which makes them more compact (see Fig. 6(b)) and increases the perturbation energy, a process known as the Orr effect, cf. Orr (1907). The circulation associated with the evolving vorticity filaments causes a displacement of the vortices visible as dipole structures at the vortex cores (Fig. 6(b)). Soon these dipoles dominate the perturbation and grow until the end of the model run (Fig. 6(c)).

A displacement of the vortices in the final state thus is the most efficient way to cause a change in the goal functionals J_V and J_E and, in case of the singular vector, to achieve a maximum perturbation energy. To interpret the structure of the dual solution it is therefore necessary to understand the displacement process. In the following we will not perform a full analysis of the perturbation evolution, but give an explanation based on previous results. For this purpose we consider the properties of optimal perturbations for barotropic vortices in shear

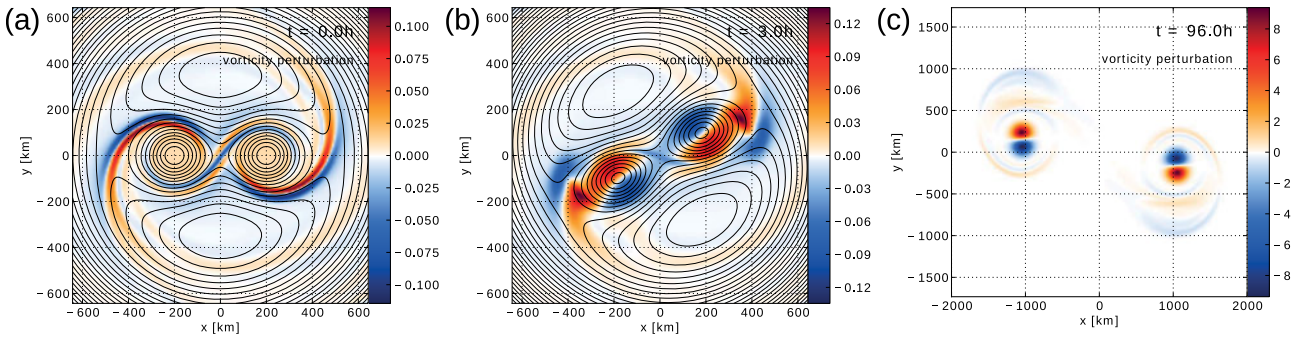

Figure 6: Time evolution of the vorticity perturbation corresponding to the adjoint sensitivity for J_E (Fig. 5(c)). The perturbation vorticity is shown at (a) $t = 0$, (b) $t = 3$ h and (c) $t = 96$ h. The black lines are streamlines in the co-rotating frame (see text).

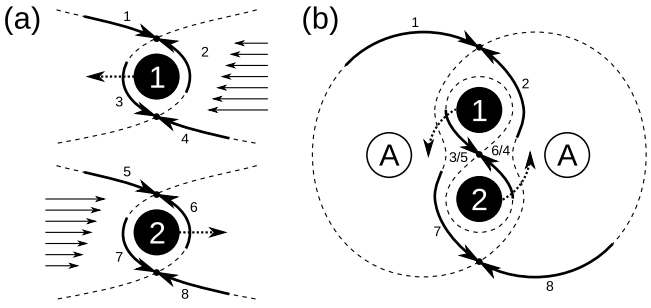

Figure 7: Schematic view of the flow structures for (a) a westward and an eastward moving cyclonic vortex steered by anticyclonic shear flows and (b) two cyclonic vortices orbiting each other. Dashed lines indicated separatrices in (a) the frames moving with each of the vortices and (b) the co-rotating frame in which the positions of the two vortices are nearly constant. Black dots are stagnation points, the solid black circles labeled "1" and "2" are cyclonic vortices, "A" indicates the positions of fictitious anticyclones arising from the transformation into the co-rotating frame. Dotted arrows show the motion of the cyclones. The black arrows show which parts of the separatrices are preferred locations for optimal perturbations and indicate the direction of the flow. The numbers indicate which separatrix sections in (a) correspond to the separatrix sections in (b).

flows discussed in Scheck et al. (2013)[6] and the flow structure for interacting vortices analysed in Melander et al. (1988).

Let us consider two interacting vortices, with vortex 1 located north of vortex 2 (Fig. 7(a)). The circulation associated with vortex 2 causes a westward directed, anticyclonic shear flow at the location of vortex 1, which will move westward. Analogously, vortex 1 causes an anticyclonic shear flow at the location of vortex 2, which moves eastward. For widely separated vortices the motion of the vortices and the direction of the shear flows is nearly zonal. North and south of each vortex stagnation points exist (black dots in Fig. 7), where in the co-moving frame the vortex circulation exactly cancels the shear flow caused by the other vortex. The dashed lines in Fig. 7 are separatrices, i.e. the streamlines in the co-moving frame that are connected to the stagnation points.

For vortices in anticyclonic shear flows the optimal perturbations are aligned with the separatrices (Scheck et al. (2013)). Perturbation vorticity is found only close to those sections of the separatrices (marked with thick black arrows) that are not too far from the stagnation points and where the flow is directed towards these stagnation points (see e.g. Fig. 5b in Scheck et al. (2013)). These locations allow perturbations to move towards the stagnation points, where they are able to maintain their position relative to the vortex centre for a long time. As discussed in Scheck et al. (2013), this has the advantage that the perturbation circulation is able to displace the vortex continuously in the same direction.

The assumption of purely zonal shear and zonal movement is not valid for the binary cyclone interaction problem considered in this study. The flow structure of this case differs significantly from Fig. 7(a) because the two vortices orbit around each other. The angular velocity of the rotation does not vary strongly in the first hours and the distance between the vortices is nearly constant. Following Melander et al. (1988), we therefore consider the streamlines in the co-rotating frame, which barely change in the first hours and allow for a clear view of the flow structure and the advection of perturbations. The flow structure in the co-rotating frame (Fig. 7(b)) can be interpreted as a superposition of the flow structures in Fig. 7(a), in which the two stagnation points between the cyclones have fused into one, plus additional effects related to the rotation of the reference frame. The transformation into the rotating frame is performed by subtracting $\frac{1}{2}\omega(x^2 + y^2)$ from the streamfunction in the non-rotating frame, where ω is the angular velocity of the co-rotating frame. As discussed by Melander et al. (1988), this transformation results in two fictitious anticyclones east and west of the cyclone pair (indicated with "A" in Fig. 7(b)). Under the influence of these anticyclones the separatrix branches 1 and 8 now connect the two outer stagnation points. Furthermore, the stagnation point between the cyclones lies on a inner separatrix that is not connected to the outer separatrices crossing at the northern and southern stagnation points. Despite of these differences, the separatrix sections cor-

[6] Scheck et al. (2013) consider the energy singular vectors. However, the adjoint sensitivity for a goal functional analogous to J_E is very similar to the leading singular vector.

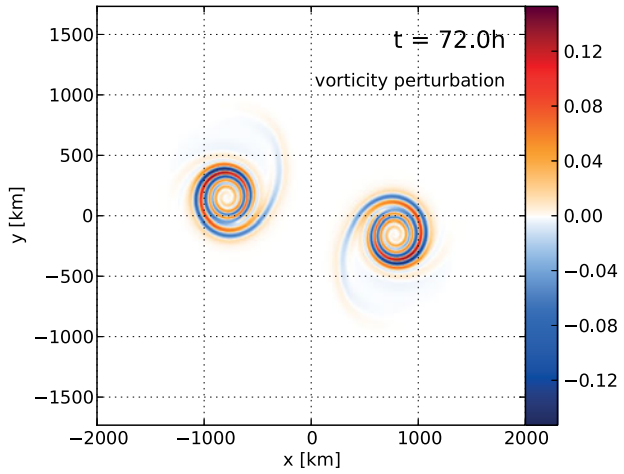

Figure 8: Adjoint vorticity for J_E at $t = 72$ h.

responding to the locations of optimal perturbations in Fig. 7(a) (thick black arrows numbered as 1 to 8) can be identified in Fig 7(b). A comparison of Fig. 7(b) with the dual solution for J_E shows that the perturbation vorticity is located exactly at the same separatrix sections. This agreement suggests that the perturbation growth mechanism in the binary cyclone interaction problem are very similar to the mechanisms identified in Scheck et al. (2013) for vortices in zonal shear flows. The alignment with separatrices allows for perturbations to grow by the Orr effect (see discussion in Scheck et al. (2013)) and accumulate at stagnation points (visible in Fig. 6(b) for the two outer stagnation points), where they are able to cause efficient displacement of the vortices.

We conclude that perturbation growth by the same processes as in Scheck et al. (2013) provides a plausible explanation of the structure of the dual solution displayed in Fig. 5. Up to now only the dual solution at $t = 0$ has been discussed. During the phase, in which the two vortices orbit around each other, the dual solution is qualitatively similar to the case $t = 0$. In the co-rotating frame the sensitive regions evolve only slowly. When the vortices separate and propagate along nearly straight tracks, the dual solution becomes similar to the optimal perturbations discussed in Nolan and Farrell (1999) and Yamaguchi et al. (2011), which are characterized by thin vorticity spirals winding around the vortex outside the radius of maximum winds (see Fig. 8 for an example). Only in the last hours the dual solution becomes restricted to the vicinity of the regions Ω_E and Ω_V, which are used in the definition of J_E and J_V, respectively. In this phase the dual solution for J_E becomes asymmetric while the one for J_V remains symmetric.

6 Adaptive numerical runs

In this section, we present adaptive numerical simulations for the binary TC interaction scenario (see Section 2.1) performed with the multi-purpose finite element library HiFlow[3], Heuveline (2010). The DWR error indicators (Section 4.2) that control the adaptation are computed using the dual solutions discussed in the previous section[7] and we apply the strategies discussed in Section 4.3 to adapt the space and time discretization. We discuss the efficiency of the adapted meshes and time partitions in comparison to uniform grids. For this purpose, the number of unknowns is considered as measure for the computational costs, while the costs related to the DWR cycles needed to construct the adapted discretization is discussed only shortly. The latter depend strongly on technical and implementation-specific aspects (e.g. adaptation strategy, possibility to re-use solutions of previous DWR cycles, availability of reduced models, etc.) and are not in the focus of this investigation.

For the assessment of the quality of the adaptive runs' solutions, we calculate a reference solution based on a mesh with 1,327,104 degrees of freedom (DOFs) in space (approx. DOF distance of 5 km) and 1,152 time steps (of length 300 s each). Based on the velocity component v_{ref} of this solution, we determined the reference values for the position of the upper left storm at time T and the three goal functionals:

$$\begin{aligned} J_{\text{Pos}}(v_{\text{ref}}) &= (-1043.7\,\text{km}, 153.4\,\text{km}), \\ J_V(v_{\text{ref}}) &= 30.74\,\text{km}^2/\text{s}, \\ J_{V,\text{ref}}(v_{\text{ref}}) &= 14.49\,\text{km}^2/\text{s}, \\ J_E(v_{\text{ref}}) &= 41.61\,\text{km}^4/\text{s}^2. \end{aligned} \tag{6.1}$$

6.1 Adaptation of the spatial mesh

In this section, we describe adaptive numerical simulations where the spatial mesh is adapted with respect to the proposed goal functionals. The time step is uniformly chosen to be 300 s and not changed during the grid adaptation. All adaptive runs are initialized on a mesh consisting of 4096 cells.

For the three goal functionals, Figures 9(a), 10(a), and 11(a) show optimized meshes with about 120,000 DOFs that fulfil the stopping criterion of the DWR method (see Section 4.3). The cell colour illustrates each cell's error contribution according to its reduced error indicator as defined in equation (4.12). Although the h-adaptivity approach (coarsening or refining of single cells) is quite flexible in comparison to alternative techniques (such as nesting for instance), the local variability of the cell sizes is limited. Besides the fact that coarsening and refining of cells changes the cell size by a factor of 4 (in two space dimensions), additional constraints due to the patch-structure and the 1-irregularity exist. For instance, sharp discontinuities in the grid resolution are not allowed. Therefore, a total balance of error indicators over all cells (i.e. all cells would have the same value) cannot be expected in general. Nevertheless, on all three meshes the cells with high indicator values (i.e.

[7] The dual solution used in adaptive runs is computed on adaptive grids, not on high-resolution uniform grids as in Section 5.

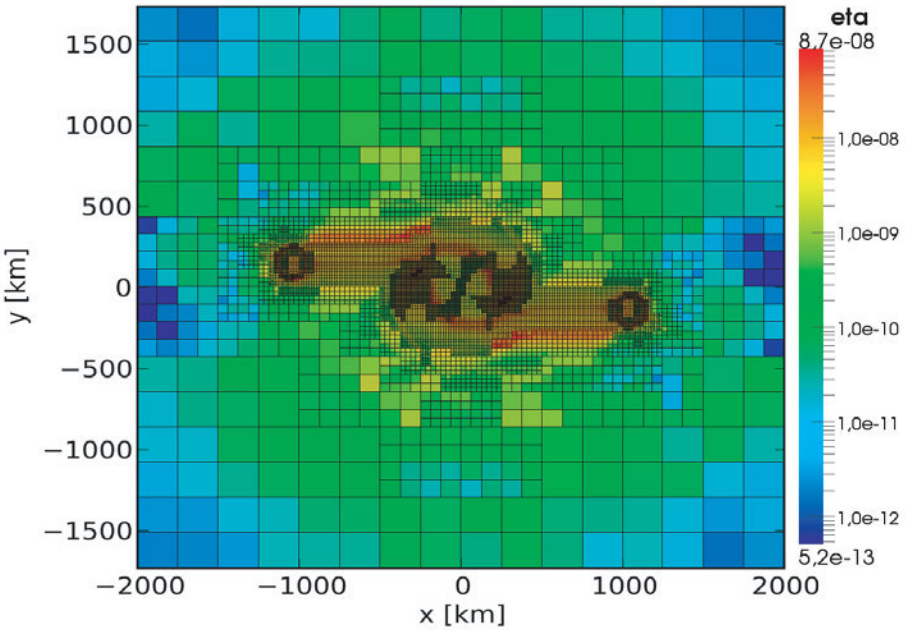

(a) Reduced error indicators on optimized grid with about 120,000 DOFs.

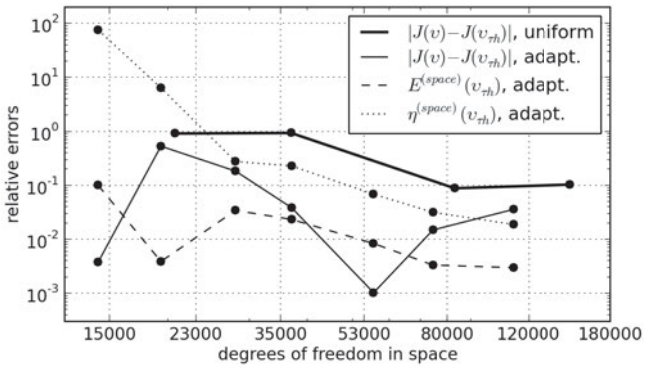

(b) Relative error in goal functional.

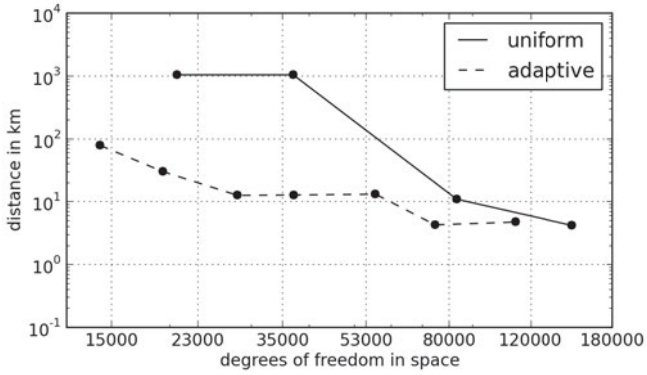

(c) Position error at time T.

Figure 9: Adapted mesh, spatial error indicators, and error quantities for functional J_V.

in the range of the largest two or three orders of magnitude) cover large parts of the domain and have both large and small sizes. This can be interpreted as evidence for a good balance of the error indicators and hence a good distribution of the cell-sizes over the mesh for all goal functionals.

The differences among these three meshes were caused by the different error indicators calculated for the respective goal functionals. A strong similarity between 9(a) and 10(a) can be discovered, reflecting that the two underlying goal functionals are defined in terms of the vorticity integral of one (the upper left) or both tropical cyclone cores at the final storm position at time T. Because of the linearity of the dual problem, its solution for the two-storm-functional J_V approximately corresponds to the superposition of the dual solution for the one-storm-functional $J_{V,\mathrm{ref}}$ with its point reflected version (in the origin). Since the grid in Fig. 10(a) is designed for the prediction of one storm only, most of the straight high-resolution section of the second storm is missing. In the last two days, the second storm moves through a rather coarse part of the grid. However, in the first two days the second storm is inside the circular high-resolution area around the domain centre also. This difference is related to the fact, that in the first two days the second storm has a large influence on the motion of the first storm, whereas in the last two days it does not. This behaviour illustrates that goal-oriented methods are able to detect automatically which features have to be well-resolved at which times to minimize the error in the goal functional. The degrees of freedom not required for the second storm can be reinvested to improve the forecast for the first storm, leading to some finer cells close to the final position of the storm and in the area of the interaction during the initial phase of development (compare Figs. 9(a) and 10(a)).

In contrast to the grids of the vorticity-based functionals, no symmetric distribution of high resolution around the final storm centre positions exist in case of J_E, see Fig. 11(a). This is in accordance with the asymmetric distribution of kinetic energy around a moving storm. As discussed in Section 5.2, the dual solution

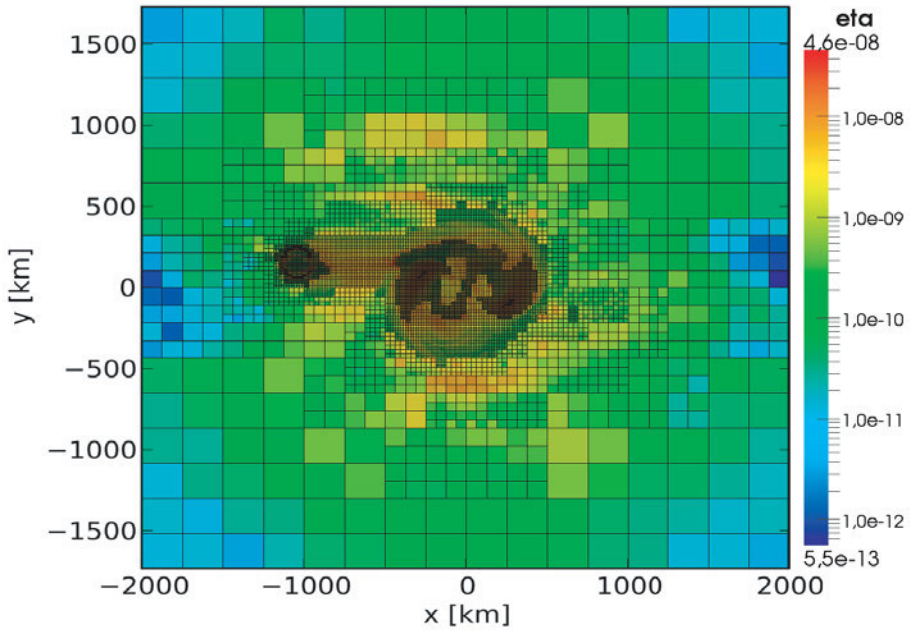

(a) Reduced error indicators on optimized grid with about 120,000 DOFs.

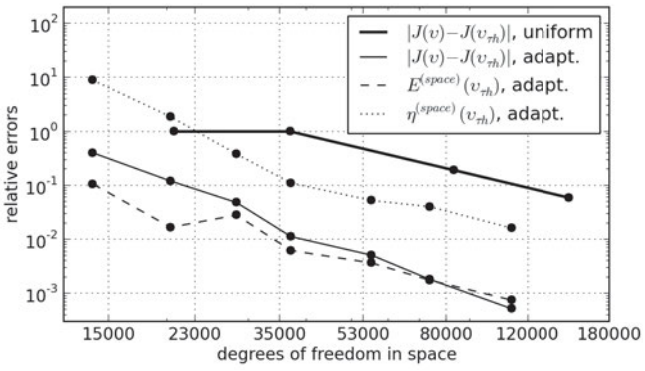

(b) Relative error in goal functional.

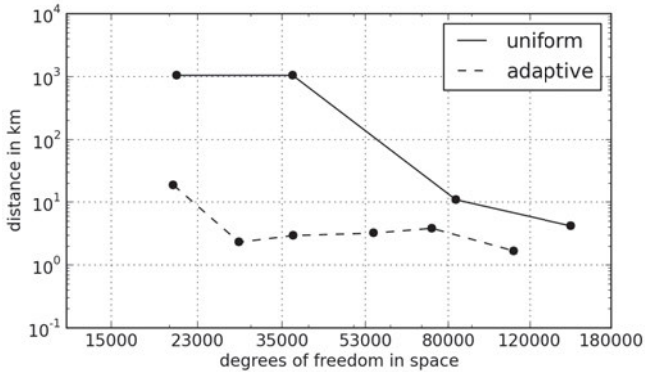

(c) Position error at time T.

Figure 10: Adapted mesh, spatial error indicators, and error quantities for functional $J_{V,ref}$.

becomes strongly asymmetric only in the last hours. Except for the asymmetric features close to the final vortex positions the high-resolution part of the grid is quite similar to the one for J_V. The stronger variation of the error indicators at larger radii in the coarser part of the grid might be caused by the additional structures in the dual solution for J_E (Fig. 5(a)), compared to the dual solution for J_V (Fig. 5(b)). These additional structures at larger radii are only present for the energy-based goal functional, because remote vorticity perturbations can have an influence on J_E (their circulation contributes to the kinetic energy near the cyclone centre), but not on J_V.

For the investigation of the efficiency of the adaptive methods, we first regard the error in the goal functional. This error measure is well-suited from a methodological point of view, since this error should be minimized by the application of the DWR method. In Fig. 10(b), the error in the goal functional $J_{V,\mathrm{ref}}$ on adapted meshes is decreased significantly compared to uniform meshes with approx. the same number of unknowns (a reduction of about two orders of magnitude). The dashed and dotted lines represent the estimated error and the summed spatial error indicators, respectively. On meshes with more than 50,000 DOFs, the estimated error is a very good approximation of the true error. However, this is no more the case for the goal functionals J_V and J_E, see Fig. 9(b) and 11(b). As described in Section 2.2, the definitions of these two functionals include the description of an integration domain which is given by means of a given approximate solution. In each DWR cycle, we redefined the goal functional based on the current approximation of the primal problem's solution which is essential to reposition the integration region to the relevant regions relative to the storm position. The ever-changing definition of the functional must be taken into account in the investigation of the error plots 9(b) and 11(b). The error in the goal functional (i.e. solid line) shows a great variability, even for the functional J_V although this is closely related to $J_{V,\mathrm{ref}}$ as the dual solutions and also the adapted meshes indicate. The dashed and dotted lines decrease asymptotically, similar to the behaviour for the functional $J_{V,\mathrm{ref}}$. This motivates a more cautious conclu-

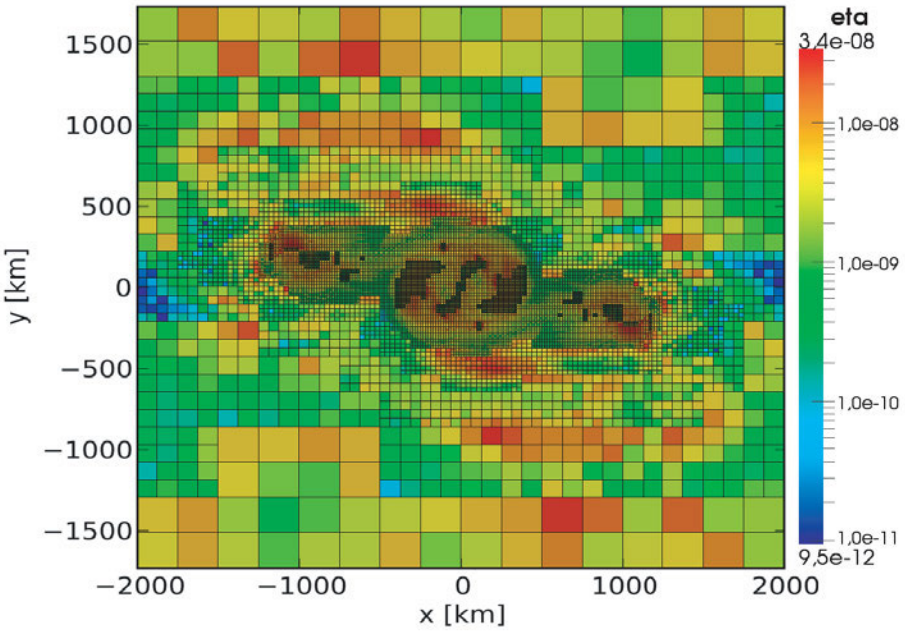

(a) Reduced error indicators on optimized grid with about 120,000 DOFs.

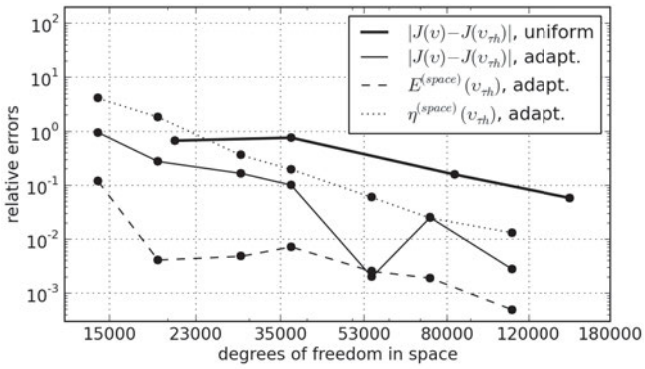

(b) Relative error in goal functional.

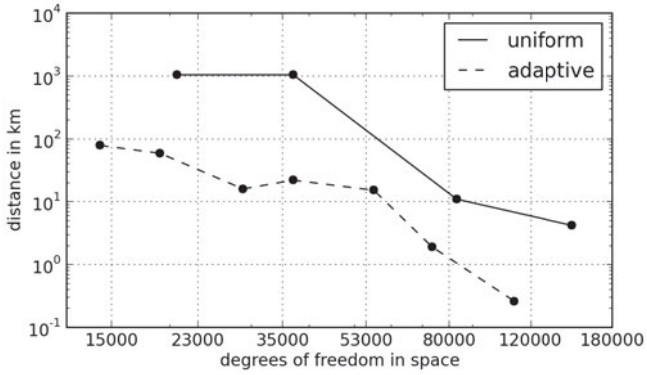

(c) Position error at time T.

Figure 11: Adapted mesh, spatial error indicators, and error quantities for functional J_E.

sion that in cases of changing definition of the goal functional, the two error quantities $E^{\text{space}}(\upsilon_{\tau h})$ and $\eta^{\text{space}}(\upsilon_{\tau h})$ are still good indications for the quality of the solution with respect to – abstractly speaking – the structures close to the storm at the final state. In summary, the error in the goal functional $J_{V,\text{ref}}$ could be reduced strongly, while for the other two functionals, the estimated error quantities indicate that the mesh adaptation lead to an adequate mesh structure, although no smooth convergence behaviour of the error in the goal functional could be detected. In this sense, at least for the functional $J_{V,\text{ref}}$ the efficiency of the adapted meshes is very high.

The error of the predicted storm position at its final state at time T is shown in the plots 9(c), 10(c), and 11(c). For the adapted meshes the storm position can be predicted qualitatively correct (i.e. the storms diverge) with a position error below 100 km even on grids with less than 20,000 DOFs. On uniform meshes with about 35,000 DOFs a qualitatively different solution is obtained, i.e. the vortices merge. This leads to a position error of about 1,000 km. Model runs based on uniform grids yield the correct, non-merging solution only for 80,000 DOFs and above. Adaptive meshes with about 30,000 DOFs lead to a position error of about 10 km for all goal functionals. Using the energy-based functional J_E, a mesh could be constructed with about 120,000 DOFs leading to a position error of less than 1 km. This suggests that the dual solution's asymmetrical structure with respect to the storm centre and the asymmetry in corresponding optimized meshes do not lead to large additional prediction errors. It must be noted that a storm position characterization in terms of the location of maximum vorticity is a delicate issue, especially on non-uniform meshes. We regularized this characterization by considering a vorticity-weighted barycentre which allows for sub-grid accuracy. Different error norms (e.g. time-averaged errors) and other characterizations of the storm position might lead to slightly different error quantities. Nevertheless, the numerical results for all goal functionals show a considerably decrease in the position error compared to uniform meshes with the same number of unknowns. Therefore, high ef-

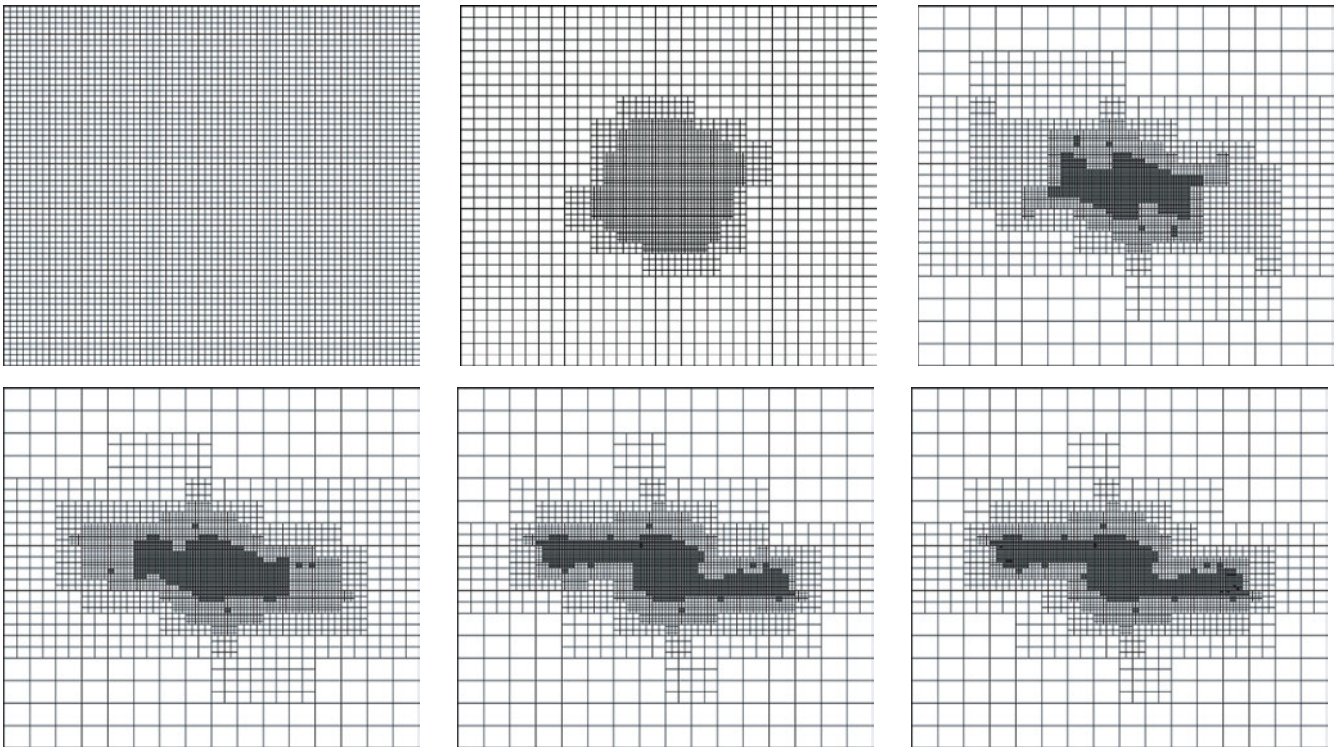

Figure 12: Sequence of meshes (corresponding to line 5 of Tab. 1) during the adaptation cycles of the DWR method for goal functional J_V for desired mesh with 6,000 cells.

Table 1: Number of desired cells (first column), number of DWR cycles of adaptive method (last column), and number of cells during DWR cycles (remaining columns) for goal functional J_V.

desir.	cyc. 1	cyc. 2	cyc. 3	cyc. 4	cyc. 5	cyc. 6	cyc. 7	cyc. 8	N
1000	4096	2032	1528	–	–	–	–	–	3
2000	4096	2608	2152	2080	–	–	–	–	4
3000	4096	2824	2920	2968	3004	–	–	–	5
4000	4096	2848	3640	3880	3940	3964	–	–	6
6000	4096	2944	5056	5704	5896	6004	–	–	6
8000	4096	2944	5872	7336	7792	7924	8032	–	7
12000	4096	2992	5968	10168	11464	11824	11980	12016	8

ficiency of the adapted meshes is given also with respect to the track prediction quality – which is the quantity of real interest that was mimicked by the proposed goal functionals.

Up to now only the end products of the grid adaptation procedure and their properties have been discussed. In the following, we give some insight into the evolution of the mesh during the adaptation procedure. As an example, the number of cells during the DWR cycles for the goal functional J_V are displayed in the Table 1. In addition, Fig. 12 shows the 6 meshes corresponding to line 5 of Tab. 1, i.e. the adaptation towards a mesh with 6,000 cells. All adaptation runs start on the same uniform mesh with 4,096 cells (i.e. 36,864 DOFs) and it takes between 3 (for coarse meshes) to 8 (for fine meshes) adaptation cycles until the stopping criterion (see Section 4.3) is reached. In the first adaptation step, the number of cells decreases strongly (up to a factor of two). For most of the runs, the number of cells in the final adapted meshes is close to the desired number of cells shown in the first row of the table (up to less than one percent of accuracy). Only for the meshes with 1,000 or 2,000 desired cells the obtained meshes consist of too many cells. This is a consequence of the stopping criterion, which aims at well-balanced error indicators but does not directly take the number of cells into account. Similar developments of the number of cells during the adaptation cycles are obtained for the goal functionals $J_{V,ref}$ and J_E.

The computational costs of the over-all procedure primarily arises from the repeated calculations of the primal and dual solution during the DWR cycles which can be estimated from the number of unknowns and the number of adaptation cycles. The rather slow convergence towards the final number of cells means that for the experiments conducted for this study the computational effort for the grid adaptation present a significant overhead. However, our adaptation strategy was not developed to minimize the total cost of the adaptation process, but to construct an efficient mesh at the end. There are several possibilities to reduce the total costs, e.g. by allowing refinement and coarsening by several levels in each adaptation cycle, which should reduce the number of cycles. Here we refrain from a detailed investigation of these possibilities, which are not in the focus of this work and could be the topic of a separate study.

The initial separation distance between the two vortices in the grid adaptation experiments is close to the

critical distance for merging. This choice allows us to study how a quite nonlinear dependence of the solution on the initial conditions influences the grid adaptation process. On the initial, uniform mesh with 4,096 cells used for the grid adaptation experiments (top left panel in Fig. 12), the numerical simulation cannot reproduce the physically correct solution in which the cyclones diverge. Instead, the two cyclones merge, which leads to a position error of more than 1,000 km (see Fig. 9(c)). Since the dual solution is based on a linearization around the primal solution in which the storms merge, the sensitivity information cannot account for the fact that the storms should diverge. Therefore, the corresponding error indicators are high only at the domain's center and lead to high resolution in this region (see second mesh in Fig. 12). Although this mesh is constructed based on the inaccurate approximate solution, it turns out that due to the increased resolution at the region of the initial interaction phase, the qualitatively correct (diverging) storm tracks can be reproduced in the next cycle. From there on, higher resolution develops at sensitive regions and especially along the correct storm tracks within the iterations.

This rather harmless impact of the bifurcation on the grid adaptation is obtained also for the goal functionals $J_{V,ref}$ and J_E. However, from these examples it cannot be concluded that there exists a general mechanism that always ensures the convergence of the adaptive method (to the knowledge of the authors no such convergence proof exists). The employed adjoint sensitivity is based on a linearization, which is meaningful only for small perturbations. For highly nonlinear problems, the sensitivity can be very inaccurate even for very small perturbations. If this issue should should slow down or prevent the convergence of the grid adaptation process for more complex test cases or models, it may be helpful to consider modified goal functionals that are not only defined at the forecast time (as the ones considered in this study), but formulated as a time integral over the full simulated time period. For such functionals, the sensitivity refers in particular also to early stages of the solution[8] where the error due to the linear approximation should be small enough to allow for a meaningful sensitivity information and thus cause grid refinement in the correct regions.

6.2 Adaptation of the time partition

In this section, we present numerical results for goal-oriented adaptation of the time-discretisation for the goal functional $J_{V,\mathrm{ref}}$. To investigate properties related to the time discretization, we fix the spatial discretization and use a pre-optimized mesh with 36,864 DOFs. We determine reduced temporal error indicators and optimize the partition of the time interval based on the adaptation strategy described in Section 4.3.

Figure 13 shows the distribution of error indicators and time step sizes on adaptive and uniform partitions consisting of 144 and 1,152 sub-intervals. The error indicators on uniform partitions (black lines in upper row) vary by several orders of magnitude within the time interval. High values can be found during the first 20 hours, where the two cyclones are closely located (phase of mutual interaction) and also on the last few hours for all partitions. Based on such error indicators, new partitions can be constructed as described in Section 4.3. The structure of optimized partitions after some DWR cycles are shown in the grey plots in the lower row of Fig. 13. In phases where error indicators of uniform meshes are large, smaller time step sizes can be found in the optimized partitions, and vice versa. The step sizes vary by a factor of approx. 10 within each partition. The resulting error indicators on the optimized partitions are plotted in the upper row of Fig. 13 in grey. The indicators are well-balanced (i.e. values correspond approximately to a fixed value) and their variability is smaller for the case of 1,152 sub-intervals.

Goal-oriented adaptation of the partition leads to remarkable improvements with respect to the different error measurements. To analyse the error due to the time-discretization, we determined a reference solution on a partition consisting of 9,216 uniform sub-intervals. By adaptation, the error in the goal functional is reduced by about one order of magnitude compared to corresponding uniform partitions, see Fig. 14(a). But the agreement of the estimated error (dashed line) and the true error in $J_{V,\mathrm{ref}}$ (thin black line) is not very good. This property might be improved by a more costly approach of a higher-order representation of the primal and dual solution during error estimation, cf. equation (4.2). The position error at time T is reduced by about one order of magnitude, see Fig. 14(b). About three-fourths of the number of sub-intervals can be saved by adaptation to achieve the same position error as using uniform partitions. Hence, the efficiency of the partition-adaptation is very high with respect to the error in the goal functional and also the position error.

A reduction in the number of time-steps corresponds roughly to the reduction in computing time of the numerical simulation. Improvements related to adaptivity in the time dimension is independent of the spatial discretization. If adaptation of the mesh is not possible or undesirable for some reason, there might yet be great potential to increase efficiency by adaptation in the time dimension.

7 Summary and conclusions

In this article, we presented a goal-oriented grid adaptation approach for efficient tropical cyclone forecasts and applied it to an idealized problem. The binary cyclone interaction used in this study presents a challenging test problem, because the solution depends sensitively and in a nonlinear way on the initial conditions and is strongly affected by numerical errors. A non-divergent barotropic model (corresponding to the incompressible

[8] In our test case: before the bifurcation.

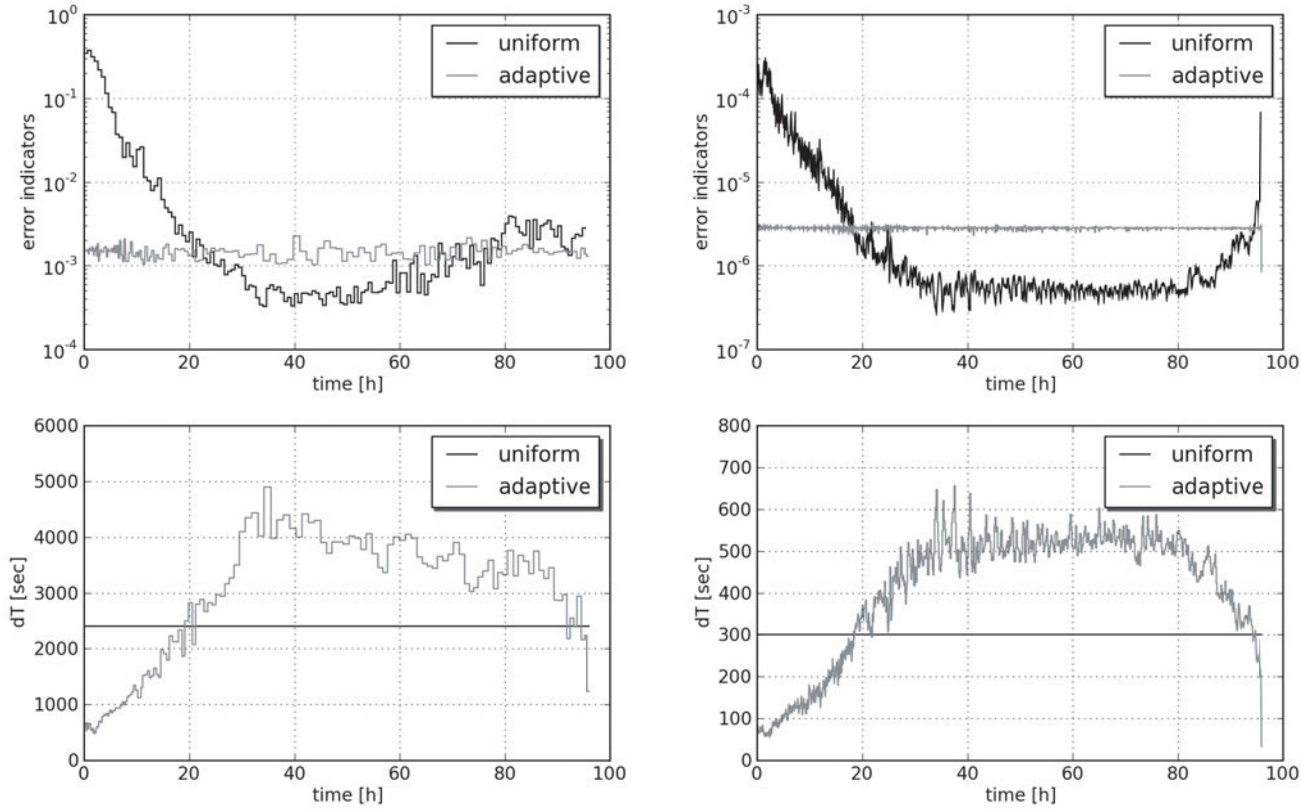

Figure 13: Error indicators (upper row) and time step sizes (lower row) on uniform and adaptive partitions of the time interval.

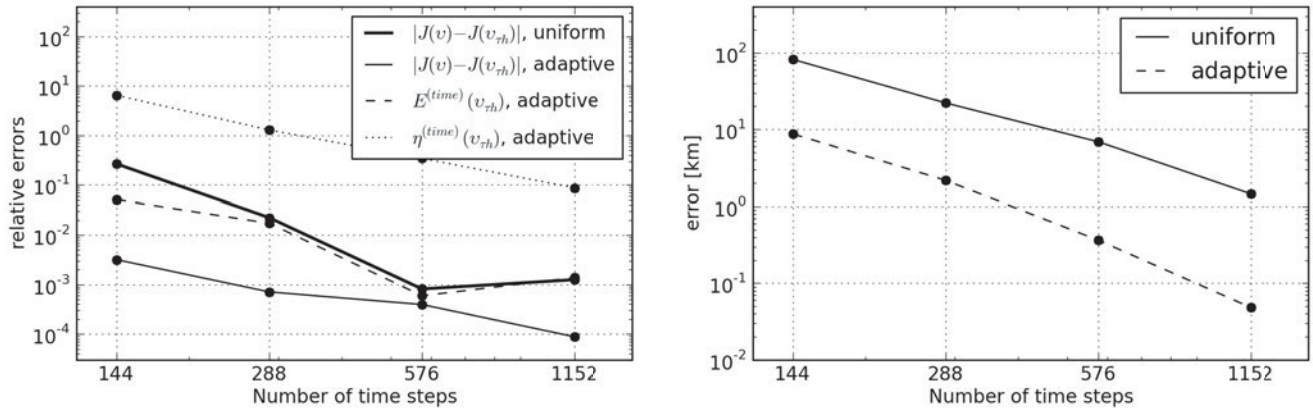

(a) Relative error in goal functional.

(b) Position error at time T.

Figure 14: Error quantities for goal functional $J_{V,\mathrm{ref}}$ on a pre-optimized spatial mesh consisting of 36,864 DOFs.

two-dimensional Navier-Stokes equations) served as an idealized description of the atmospheric dynamics. For the numerical solution we used a space-time finite element method. The discrete solutions are Galerkin projections with respect to the space and the time discretization and are suitable for goal-oriented error estimation in the framework of the DWR method. This method allows for automatic grid adaptation with the aim of minimizing the error in a user-defined goal functional. For this purpose, a linear sensitivity analysis is carried out, which identifies the cells having the largest influence on the goal functional. We investigated several physically motivated goal functionals that are correlated with the storm position and computed the associated sensitivity information in form of the dual solution. The adjoint-based sensitivity often used in meteorological applications was identified as a special case of the dual solution. The structure of the dual solution for the binary TC interaction scenario could be explained by interpreting it as an optimal perturbation, which grows by mechanisms similar to the ones identified for vortices in shear flows. We proposed an a posteriori error estimator for these goal functionals, derived separate error indicators for the space- and time-dimension, and developed

strategies for the adaptation of the mesh and the time-partition. We constructed optimized meshes for the tropical cyclone scenario by refining and coarsening cells (i.e. h-adaptivity) and optimized partitions of the time-interval. This resulted in well-balanced spatial error indicators over the cells and almost optimally distributed temporal error indicators over the intervals of the time partition. In a series of numerical tests on adapted and uniform grids, we compared the error related to both the goal functionals and also the predicted storm position. For a fixed number of DOFs, the adapted grids lead to significantly reduced errors in both norms. For spatially adapted configurations with low number of unknowns, the error in the position error was reduced by about two orders of magnitude. For a given number of time steps, the adaptation of the time partitioning resulted in a reduction of the error by another order of magnitude. In this sense, these discretizations are therefore highly efficient.

For the scenario under investigation, the efficiency could significantly be increased by goal-oriented adaptation of the time partition. This demonstrates the great potential of adaptivity in the time-dimension which can be achievable even if the mesh can not or should not be adapted. The temporal error indicators (4.10) quantify each cell's contribution to the error related to the time-discretization for any cell in the space-time mesh. From these, we derived reduced error indicators (4.13) to adapt mesh-global time steps instead of adopting adaptivity on the level of the space-time mesh directly. The perspective of a Cartesian product of one spatial mesh and one partition of the time interval involves strong limitations with respect to adaptivity, but already allowed for considerably efficiency improvements. Future investigations should address more flexible adaptivity techniques including dynamic mesh adaptation. In the context of such space-time finite element methods, the consideration of a space-dependent time-discretization (e.g. varying time-step sizes or locally higher-order methods for the time-discretization) controlled by goal-oriented error indicators seems to be promising.

In this article, efficiency was defined in terms of quality (either error in goal functional or error in storm position) and the number of unknowns on optimized discretizations. We did not take the required CPU time into account, which depends strongly on the implementation (e.g. applied data structures, solvers, availability of reduced models, etc.), on the available hardware, and on the adaptation strategy (i.e. the way how error indicators control the mesh adaptation). Investigating the efficiency of the full adaptive method is beyond the scope of this study. However, ultimately the computational costs related to repeated calculations of sensitivity, error estimation, and corresponding adaptation must be included in the efficiency investigation to clarify whether the adaptive method is able to improve the efficiency of the overall computation. The goal-oriented approach requires substantial computational resources for the error estimation, primarily because it involves a linear sensitivity analysis that allows for a detection of regions that are important for the development of the storm. There are alternative, computationally cheaper methods, e.g. error estimators in global norms, which do not rely on sensitivity information. However, the inability to detect remote regions that could have a large impact on the development of the storm could be a serious problem for these cheaper methods. We plan to compare the goal-oriented approach and these alternative methods in a future study.

The computational overhead associated with goal-oriented grid adaptation could be reduced also, for instance by using a model of reduced complexity for the error estimation. Sensitivity information is computed on relatively coarse grids in operational weather forecasting centers and used successfully for meteorological applications like the definition of ensemble perturbations. This suggests that computationally cheaper models could be sufficient also for the error estimation required in the grid adaptation process. The results of Bauer et al. (2014) present an argument in favour of the feasibility of this approach. They demonstrate that error estimates obtained with a finite element model can be used successfully to control the grid adaptation in a finite difference model, even in the case where the two model equations are not exactly the same. Furthermore, they show that considerable gains in efficiency can be achieved even if grid adaptation is applied only as pre-processing step and not implemented as an iterative process. With similar solutions, efficiency gains might be achievable even in cases where some components (e.g. the adjoint model) needed for rigorous a posteriori error estimation do not exist. Such approaches represent important steps towards goal-oriented adaptivity for more realistic tropical cyclone forecast models.

In this study we considered two physically equally well-motivated goal functionals based on regions of high kinetic energy or high vorticity. Both of them are strongly correlated with the storm positions and resulted in highly efficient grids. An analysis of the dual solutions indicated that the most efficient way to change the value of the goal functionals is in both cases to move the storm, and the optimal perturbations causing a displacement of the storm are basically the same in both cases. Furthermore, the fact that the energy-based functional introduced an artificial asymmetry in the solution did not result in obvious problems, because this asymmetry in the grid became evident only at the very end of the simulated time span. These results indicate that at least in the barotropic case finding an adequate goal functional for the prediction of tropical storms is not a major problem. An investigation of goal functionals for more realistic, three-dimensional models including moisture could start from a generalization of these goal functionals. We also investigated the case where only one of the two storms is of interest and included in the goal functional. This case illustrates the possibility of the goal-oriented approach to focus on a specific feature. It would be also possible to consider more than one feature by using the sum of several goal functionals. This would e.g. allow for the

enhanced representation of features that are not important for the storm itself, but depend on the storm and are relevant forecast goals. Remote heavy precipitation events triggered by tropical storms are an example for such a feature.

In this study we consider only the discretization error, which is an important contribution to the model error, and its impact on the forecast. An even more challenging problem for numerical weather prediction is the inherent uncertainty in the initial state and the boundary conditions. Probabilistic forecasts take these uncertainties into account by employing ensembles of model runs. In general the differences between the independently evolving ensemble members become too large to describe them by a linear model like the discretized dual problem used in this study. Although the methods used here can thus not be applied directly to account for the uncertainty, extensions to this approach that will address uncertainty are in development. One first study in this new field of research that focuses on stochastic advection-diffusion problems, cf. Almeida and Oden (2010), involves an adaptive algorithm that adjusts the probabilistic grid and the discretization error. To our knowledge, such methods have not been applied to complex atmospheric model systems yet, but represent promising approaches that could lead to major advancements in probabilistic numerical weather prediction.

Even without such comprehensive concepts that directly involve the uncertainty, TC forecasts could benefit from the fact that the sensitivity with respect to the goal functional, the dual solution, is a free by-product of the error estimation process. This information could be helpful in reducing the uncertainty in the initial state. For instance, it could be used to determine where additional observations should be carried out (targeted observations). The assimilation of these observations will specifically reduce the fastest-growing errors. Moreover, also in the data assimilation process itself adjoint models are required (e.g. for the 4DVar method used at ECMWF) or could be beneficial, see e.g. Zhang and Zhang (2012). Obtaining information comparable to the dual solution (e.g. in form of adjoint sensitivity or singular vectors) usually requires significant additional effort. Thus, goal-oriented adaptivity can provide more than just optimized meshes and for a fair comparison with other grid refinement methods this advantage should be taken into account.

Appendix

In the following, the notations for the continuous and discrete function spaces that are used in this article are outlined.

The continuous function spaces

As is customary in literature, the space of squared Lebesque measurable functions is denoted by $L^2(\Omega)$ with the inner product $(a,b) = \int_\Omega a(x) \cdot b(x)\,dx$ and the two-dimensional variant $H := L^2(\Omega)^2$. For the pressure variable we introduce the function space $Q := \{p \in L^2(\Omega) \,|\, \int_\Omega p(x)\,dx = 0\}$. For the velocity variable the space of vector-valued functions with distributional derivatives that fulfil the periodicity condition (3.2) additionally is introduced and denoted by $V := H^1_p(\Omega)^2$ with dual space V^*.

For the time-dependent functions, we introduce the following notation for arbitrary Banach spaces B (e.g. H or V). The space of functions $f : [0,T] \to B$ for which $\int_0^T \|f(t)\|_B^p\,dt < \infty$ for $p \in [0,\infty)$ is denoted $L^p(0,T;B)$. Similarly, $L^\infty(0,T;B)$ denotes the space of functions for which $M > 0$ exists such that $\|f(t)\|_B \le M$ for almost all $t \in [0,T]$. With these notations, the functions spaces for the continuous primal and dual problem (3.3) and (3.4) are

$$\begin{aligned} X &:= \{\upsilon \in L^4(0,T;V) \,|\, \partial_t \upsilon \in L^2(0,T;V^*)\} \\ &\quad \cap\ L^\infty(0,T;H), \\ Y &:= L^2(0,T;V) \cap L^\infty(0,T;H), \\ M &:= L^2(0,T;Q), \end{aligned}$$

Since functions in X are almost everywhere equal to a continuous function in time, Emmrich (2004), the initial condition for the velocity is meaningful. Further details on the function spaces and the presented variational formulations can be found e.g. in Emmrich (2004); Temam (2001).

The discrete function spaces

For the spatial finite element discretization, corresponding function spaces for the velocity variable, $V_h \subseteq V$, and for the pressure variable, $Q_h \subseteq Q$, are defined by

$$\begin{aligned} V_h &:= \left\{\upsilon_h \in C(\Omega)^2 \,|\, \upsilon_{h|K} \in Q_2(K)^2\ \forall K \in \mathcal{T}_h\right\}, \\ Q_h &:= \{p_h \in C(\Omega) \,|\, p_{h|K} \in Q_1(K)\ \forall K \in \mathcal{T}_h\}. \end{aligned}$$

Here, $Q_m(K)$ denotes polynomials of maximum degree $m \ge 0$ in each variable defined on cell $K \in \mathcal{T}_h$ which in two space dimensions has the form

$$Q_m(K) := \{q : K \to \mathbb{R} \,|\, q(x,y) = \sum_{0 \le s,t \le m} q_{st} x^s y^t\},$$

for $q_{st} \in \mathbb{R}$ and $(x,y) \in K$. Global continuity of the function spaces V_h and Q_h can easily be guaranteed by simple interpolation conditions, as described e.g. in Heuveline and Schieweck (2007).

For the discretization in time, we consider B-valued functions (B being some arbitrary function space) that are defined on the interval $I = [0,T]$ and assume a partitioning of the form $0 = t_0 < t_1 < \ldots < t_N = T$. We introduce functions that are polynomials of order k

on each sub-interval $(t_{i-1}, t_i) \subset I$:

$$\mathbb{P}_k^{dc}(B) := \{ f : I \to B \,|\, f_{|(t_{i-1},t_i)}(t) = \sum_{n=0}^{k} f_n t^n \quad \forall t \in (t_{i-1}, t_i),\ f_n \in B,\ 1 \le i \le N \}.$$

These functions may be discontinuous at all points in time t_i. We introduce additionally the corresponding space of continuous functions by intersection with the space of globally continuous functions, i.e.

$$\mathbb{P}_k^{c}(B) := \mathbb{P}_k^{dc}(B) \cap C([0,T]; B),$$

which is used for the trial functions of the velocity variable.

Acknowledgements

The authors acknowledge support from the DFG priority programme SPP-1276 MetStröm: Multiple Scales in Fluid Mechanics and Meteorology (participating support codes JO306/6-2 and HE4760/3-3).

References

Ainsworth, M., J.T. Oden, 2000: A Posteriori Error Estimation in Finite Element Analysis. – John Wiley & Sons Inc., 240 pp.

Almeida, R.C., J. Oden, 2010: Solution verification, goal-oriented adaptive methods for stochastic advection-diffusion problems. – Comput. Methods Appl. Mech. Eng. **199**, 2472–2486.

Babuška, I., W. Rheinboldt, 1978: Error estimates for adaptive finite element computation. – SIAM J. Num. Anal. **15**, 736–754.

Bangerth, W., R. Rannacher, 2003: Adaptive Finite Element Methods for Differential Equations. – Birkhäuser Verlag, 208 pp.

Bauer, W., M. Baumann, L. Scheck, A. Gassmann, V. Heuveline, S. Jones, 2014: Simulation of tropical-cyclone-like vortices in shallow-water icon-hex using goal-oriented r-adaptivity. – Theor. Comp. Fluid Dyn. **28**, 107–128.

Baumann, M., 2011: Numerical Simulation of Tropical Cyclones using Goal-Oriented Adaptivity. – Ph.D. Thesis, Universität Karlsruhe (TH), Karlsruhe, Germany.

Beckers, M., H.J.H. Clercx, G.J.F. van Heijst, R. Verzicco, 2002: Dipole formation by two interacting shielded monopoles in a stratified fluid. – Phys. Fluids **14**, 704–720.

Birchfield, G.E., 1960: Numerical prediction of hurricane movement with the use of a fine grid. – J. Meteor. **17**, 406–414.

Braack, M., R. Rannacher, 1999: Adaptive finite element methods for low-mach-number flows with chemical reactions. – In: 30th Computational Fluid Dynamics, von Karman Institute, 1–93.

Brand, S., 1970: Interaction of binary tropical cyclones of the western north pacific ocean. – J. Appl. Meteorol. (JAM) **9**, 433–441.

Brezzi, F., 1974: On the existence, uniqueness, and approximation of saddle point problems arising from Lagrangian multipliers. – Rev. Fr. Automat. Infor. **8**, 129–151.

Brezzi, F., R.S. Falk, 1991: Stability of higher-order Hood-Taylor methods. – SIAM J. Numer. Anal. **28**, 581–590.

Cavallo, S.M., R.D. Torn, C. Snyder, C. Davis, W. Wang, J. Done, 2013: Evaluation of the advanced hurricane wrf data assimilation system for the 2009 atlantic hurricane season. – Mon. Wea. Rev. **141**, 523–541.

Davis, C., G. Holland, 2007: Realistic simulations of intense hurricanes with the ncep/ncar wrf modeling system. – 10th International Workshop on Wave Hindcasting and Forecasting and Coastal Hazard Symposium, North Shore, Hawaii.

Dong, K., C.J. Neumann, 1983: On the relative motion of binary tropical cyclones. – Mon. Wea. Rev. **111**, 945–953.

Dritschel, D.G., D.W. Waugh, 1992: Quantification of the inelastic interaction of unequal vortices in two-dimensional vortex dynamics. – Phys. Fluids **4A**, 1737–1744.

Emmrich, E., 2004: Gewöhnliche und Operator-Differentialgleichungen: Eine integrierte Einführung in Randwertprobleme und Evolutionsgleichungen für Studierende. – Vieweg & Teubner, Wiesbaden, 316 pp.

Eriksson, K., C. Johnson, 1991: Adaptive finite element methods for parabolic problems i: A linear model problem. – SIAM J. Num. Anal. **28**, 43–77.

Eriksson, K., D. Estep, P. Hansbo, C. Johnson, 1995: Introduction to Adaptive Methods for Differential Equations. – Acta Numer. **4**, 105–158.

Errico, R.M., 1997: What is an adjoint model?. – Bull. Amer. Meteor. Soc. **78**, 2577–2591.

Fujiwhara, S., 1921: The natural tendency towards symmetry of motion and its application as a principle of motion. – Quart. J. Roy. Meteor. Soc. **47**, 287–293.

Fujiwhara, S., 1923: On the growth and decay of vortical systems. – Quart. J. Roy. Meteor. Soc. **49**, 75–104.

Fujiwhara, S., 1931: Short note on the behaviour of two vortices. – Proc. Phys. Math. Soc. Japan, Ser. 3 **13**, 106–110.

Fulton, S.R., 2001: An adaptive multigrid barotropic tropical cyclone track model. – Mon. Wea. Rev. **129**, 138–151.

Giering, R., T. Kaminski, 1998: Recipes for Adjoint Code Construction. – ACM Trans. On Math. Software **24**, 437–474.

Harrison, E.J., R.L. Elsberry, 1972: A method for incorporating nested finite grids in the solution of systems of geophysical equations. – J. Atmos. Sci. **29**, 1235–1245.

Heuveline, V., 2010: HiFlow3: A flexible and hardware-aware parallel finite element package. – In: Proceedings of the 9th Workshop on Parallel/High-Performance Object-Oriented Scientific Computing, POOSC '10, 4:1–4:6, New York, NY, USA. ACM.

Heuveline, V., R. Rannacher, 2006: Adaptive FEM for Eigenvalue Problems with Application in Hydrodynamic Stability Analysis. – Advances in Numercial Mathematics, Proc. Int. Conf., Sept. 16–17, 2005, Moscow, 1–32.

Heuveline, V., F. Schieweck, 2007: On the inf-sup condition for higher order mixed fem on meshes with hanging nodes. – M2AN **41**, 1–20.

Hinze, M., R. Pinnau, M. Ulbrich, S. Ulbrich, 2008: Optimization with PDE Constraints. – Springer, 270 pp.

Holland, G.J., G.S. Dietachmayer, 1993: On the interaction of tropical-cyclone-scale vortices. iii. Continuous barotropic vortices. – Quart. J. Roy. Meteor. Soc. **119**, 1381–1398.

Jarrell, J.D., S. Brand, D.S. Nicklin, 1978: An analysis of western north pacific tropical cyclone forecast errors. – Mon. Wea. Rev. **106**, 925–937.

Lander, M., G.J. Holland, 1993: On the interaction of tropical-cyclone-scale vortices. i: Observations. – Quart. J. Roy. Meteor. Soc. **119**, 1347–1361.

Melander, M.V., J.C. McWilliams, N.J. Zabusky, 1987: Axisymmetrization and vorticity-gradient intensification of an isolated two-dimensional vortex through filamentation. – J. Fluid Mech. **178**, 137–159.

Melander, M.V., J.C. McWilliams, N.J. Zabusky, 1988: Symmetric vortex merger in two dimensions: causes and conditions. – J. Fluid Mech. **195**, 303–340.

Nolan, D.S., B.F. Farrell, 1999: Generalized stability analyses of asymmetric disturbances in one- and two-celled vortices maintained by radial inflow. – J. Atmos. Sci. **56**, 1282–1307.

Orr, W.M., 1907: Stability or instability of the steady motions of a perfect liquid. – Proc. Roy. Irish Acad. **27**, 9–69.

Peng, M.S., C.A. Reynolds, 2006: Sensitivity of tropical cyclone forecasts as revealed by singular vectors. – J. Atmos. Sci. **63**, 2508–2528.

Prieto, R., B.D. McNoldy, S.R. Fulton, W.H. Schubert, 2003: A classification of binary tropical cyclone-like vortex interactions. – Mon. Wea. Rev. **131**, 2656–2666.

Reynolds, C.A., M.S. Peng, J.-H. Chen, 2009: Recurving tropical cyclones: Singular vector sensitivity and downstream impacts. – Mon. Wea. Rev. **137**, 1320–1337.

Richter, A., 2012: Untersuchungen zur Wechselwirkungg tropischer Wirbelstürme mit Hilfe eines idealisierten dreidimensionalen numerischen Modells. –Diploma Thesis, Institute for Meteorology and Climate Research, Karlsruhe Institute of Technology, Germany.

Ritchie, E.A., G.J. Holland, 1993: On the interaction of two tropical cyclone scale vortices. ii: Discrete vortex patches. – Quart. J. Roy. Meteor. Soc. **119**, 1363–1379.

Scheck, L., S.C. Jones, M. Juckes, 2011a: The resonant interaction of a tropical cyclone and a tropopause front in a barotropic model, Part I: Zonally-oriented front. – J. Atmos. Sci. **68**, 405–419.

Scheck, L., S.C. Jones, M. Juckes, 2011b: The resonant interaction of a tropical cyclone and a tropopause front in a barotropic model, Part II: Frontal waves. – J. Atmos. Sci. **68**, 420–429.

Scheck, L., S.C. Jones, V. Heuveline, 2013: Singular vectors for barotropic, hurricane-like vortices in horizontal shear: Structure and perturbation growth mechanisms. – J. Atmos. Sci. **71**, 1002–1020, doi:10.1175/JAS-D-13-0226.1

Schieweck, F., 2010: A-stable discontinuous Galerkin-Petrov time discretization of higher order. – J. Numer. Math. **18**, 25–57.

Schmich, M., B. Vexler, 2007: Adaptivity with dynamic meshes for space-time finite element discretizations of parabolic equations. – SIAM J. Sci. Comput. **30**, 369–393.

Shin, S.-E., J.-Y. Han, J.-J. Baik, 2006: On the critical separation distance of binary vortices in a nondivergent barotropic atmosphere. – J. Meteor. Soc. Japan **84**, 853–869.

Smith, R.K., W. Ulrich, G. Dietachmayer, 1990: A numerical study of tropical cyclone motion using a barotropic model. I: The role of vortex asymmetries. – Quart. J. Roy. Meteor. Soc. **116**, 337–362.

Temam, R., 2001: Navier-Stokes equations: Theory and Numerical Analysis. – AMS Chelsea Publ., Providence, RI.

Valcke, S., J. Verron, 1997: Interactions of baroclinic isolated vortices: The dominant effect of shielding. – J. Phys. Oceanogr. **27**, 524–541.

Yamaguchi, M., D.S. Nolan, M. Iskandarani, S.J. Majumdar, M.S. Peng, C.A. Reynolds, 2011: Singular Vectors for Tropical Cyclone-Like Vortices in a Nondivergent Barotropic Framework. – J. Atmos. Sci. **68**, 2273-2291.

Zhang, M., F. Zhang, 2012: E4dvar: Coupling an ensemble kalman filter with four-dimensional variational data assimilation in a limited-area weather prediction model. – Mon. Wea. Rev. **140**, 587–600.